AD-A160 151 MECHANICS OF A TWO AXES PASSIVE PRECISION LEVEL MONITOR FOR MACHINE TOOLS VOLUME 2(U) PURDUE UNIV LAFAYETTE IN J D YORK ET AL. MAY 85 N00014-83-K-0385 1/2

UNCLASSIFIED F/G 14/2 NL

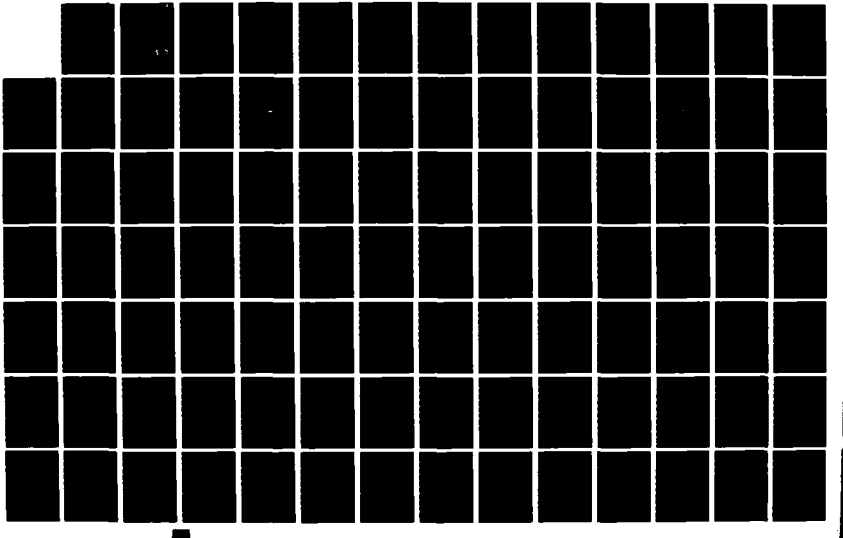

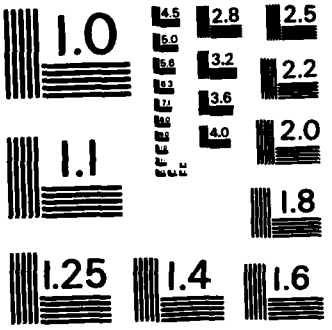

THE SCIENCE OF AND ADVANCED TECHNOLOGY FOR COST—EFFECTIVE MANUFACTURE OF HIGH PRECISION ENGINEERING PRODUCTS

ONR Contract No 83K0385
FINAL REPORT
VOL. 2

MECHANICS OF TWO AXES PASSIVE PRECISION LEVEL MONITOR FOR MACHINE TOOLS

PREPARED BY
J. D. York and J. Modrey

MAY 1985

Schools of
Mechanical, Industrial, and Electrical Engineering
Purdue University
West Lafayette, Indiana 47907

None
SECURITY CLASSIFICATION OF THIS PAGE

REPORT DOCUMENTATION PAGE

1a. REPORT SECURITY CLASSIFICATION None	1b RESTRICTIVE MARKINGS None
2a SECURITY CLASSIFICATION AUTHORITY None	3 DISTRIBUTION/AVAILABILITY OF REPORT This document has been approved for public release and sale; its distribution is unlimited.
2b DECLASSIFICATION / DOWNGRADING SCHEDULE None	
4. PERFORMING ORGANIZATION REPORT NUMBER(S) Final Report Vol. 2	5. MONITORING ORGANIZATION REPORT NUMBER(S)
6a. NAME OF PERFORMING ORGANIZATION PURDUE UNIVERSITY 6b. OFFICE SYMBOL (If applicable)	7a NAME OF MONITORING ORGANIZATION Department of Defense Office of Naval Research
6c. ADDRESS (City, State, and ZIP Code) School of Industrial Engineering West Lafayette, IN 47907	7b ADDRESS (City, State, and ZIP Code) Arlington, VA 22217-5000
8a. NAME OF FUNDING / SPONSORING ORGANIZATION 8b. OFFICE SYMBOL (If applicable) 614A	9 PROCUREMENT INSTRUMENT IDENTIFICATION NUMBER N00014-83-K-0385/12/12
8c ADDRESS (City, State, and ZIP Code)	10 SOURCE OF FUNDING NUMBERS PROGRAM ELEMENT NO: ONR:433 / PROJECT NO: / TASK NO: SRO-150 / WORK UNIT ACCESSION NO:

11 TITLE (Include Security Classification)
MECHANICS OF A TWO AXES PASSIVE PRECISION LEVEL MONITOR FOR MACHINE TOOLS

12 PERSONAL AUTHOR(S)
York, J. D. and J. Modrey

13a. TYPE OF REPORT	13b. TIME COVERED	14 DATE OF REPORT (Year, Month, Day)	15. PAGE COUNT
Final	FROM 1-1-83 TO 6-1-84	May 1985	106

16 SUPPLEMENTARY NOTATION

17 COSATI CODES			18 SUBJECT TERMS (Continue on reverse if necessary and identify by block number)
FIELD	GROUP	SUB-GROUP	Collimator, Precision level, Spherical pendulum, Precisic engineering, Linkage mechanisms
13			

19. ABSTRACT (Continue on reverse if necessary and identify by block number)

A mechanism is proposed as a means of passively leveling an optical assembly about two horizontal axes within a tolerance of one arc-second. The mechanism is designed so that it will stimulate a spherical pendulum for input motions up to 100 arc-seconds. In order to insure the operation of the mechanism and establish the proper geometry, three analytical models were developed. Planar and spatial models which assumed rigid links with pin joints and a planar model assuming deformable links with pin and clamped joints were studied. These results are compared with experimental data gathered for three geometry combinations.

It is shown that the results from the planar and spatial analytics agree to within 10%, with the spatial model predicting less error. Hence, the less complicated planar analysis may be performed with little loss in accuracy. Neither rigid link models compare well with the experimental data, with as much as an 80% discrepancy in some cases. When deformable links are included in the planar model, the results are within 16% of the experimental results. This indicates that the resistance to bending at the points can not be neglected in modeling and mechanism to act like a spherical pendulum, and guidelines are established for the design.

20 DISTRIBUTION / AVAILABILITY OF ABSTRACT	21 ABSTRACT SECURITY CLASSIFICATION
☐ UNCLASSIFIED/UNLIMITED ☒ SAME AS RPT ☐ DTIC USERS	None
22a NAME OF RESPONSIBLE INDIVIDUAL Dr. David Mizell, Scientific Officer	22b TELEPHONE (Include Area Code) (818) 795-5971 x 56
22c OFFICE SYMBOL 433	

DD FORM 1473, 84 MAR — 83 APR edition may be used until exhausted. All other editions are obsolete

SECURITY CLASSIFICATION OF THIS PAGE
None

THE SCIENCE OF AND ADVANCED TECHNOLOGY FOR COST-EFFECTIVE MANUFACTURE OF HIGH PRECISION ENGINEERING PRODUCTS

ONR Contract No. 83K0385
Final Report
Vol. 2

MECHANICS OF A TWO AXES PASSIVE PRECISION LEVEL MONITOR FOR MACHINE TOOLS

Prepared by
J. D. York and J. Modrey

May 1985

Schools of
Mechanical, Industrial and Electrical Engineering
Purdue University
West Lafayette, Indiana 47907

This report represents, with minor changes, the thesis submitted by Mr. James York to the Faculty of Purdue University for the award of the Degree of Master of Science in Mechanical Engineering.

Research described in this report has been supported by the Office of Naval Research through Contract No. N83K0385 in the framework of the ONR Precision Engineering projects.

Dr. Joseph Modrey, Co-Principal Investigator in the project served as Major Professor for the thesis.

Work on the Precision Engineering project at Purdue University greatly benefited from the use of the technical facilities of the Purdue Computer Integrated Design, Manufacturing and Automation Center (CIDMAC) and the advice of the CIDMAC member companies*.

Moshe M. Barash
Principal Investigator

C. Richard Liu
Principal Investigator

*Member companies of CIDMAC are:
Cincinnati Milacron; TRW; Ransburg Corporation; Cummins Engine Co.; Control Data Corporation; ALCOA which is gratefully acknowledged.

TABLE OF CONTENTS

LIST OF TABLES

LIST OF FIGURES

LIST OF SYMBOLS

Symbols for Chapters 1 to 5

β: $= \frac{P}{EI}$

A_x, A_y, A_z: Coordinates of pin joint A

C_1, C_2, C_3, C_4: Integration Constants

Δ: Distance along link from center of gravity (G) to the middle of the output link (L/2) (Figure 2.1)

δ: Input link length

E: Modulus of elasticity

$\bar{e}_{A/C}$: Unit vector from C to A

ε: Vertical distance from center of gravity (G) to the ouput link (Figure 2.1)

f_{AC}: Magnitude of force exerted on C by A (Figure 2.2)

H_{ℓ}: Shear force at point ℓ (Figure 4.4)

h: Height of mechanism measured from center of input link vertically to center of output link (Figure 2.1)

I: Moment of inertia

K: Output / Input ratio

L: Output link length

ℓ_{AC}: Link length from A to C

m: Mass of optics and ouput link

M_ℓ: Moment at point ℓ (Figure 4.4)

P: Axial force along cable (Figure 4.4)

$\bar{R}_{C/A}$: Vector from C to A

θ_A, θ_B: Angles made by undeflected cables from vertical (Figure 4.1)

θ_i: Input angle

θ_o: Output angle

u: Coordinate along undeflected cable (Figure 4.3)

w: Deflection of cable (Figure 4.3)

Symbols for Chapter 6

C_D: Damping constant

c: Radial clearance, $c = R_o - R_i$

D: $\dfrac{h_o}{12V\mu_o\ell^2}$

e: Displacement of center

ε: $\dfrac{e}{c}$

H: $\dfrac{h}{h_o}$

h: Gap at a point along the damper

h_o: Gap at bottom of damper

J: Mass moment of inertia of assembly about O

k: Radius of gyration of total pendulum

L: Pendulous length to bottom edge of damper

$\bar{L}$: Pendulum length to center of gravity (G)

L_D: Pendulum length to center of damper action

ℓ: Effective length of cylindrical damper

m: Mass of total pendulum

μ: Viscosity

P: $\frac{p}{D}$

ϕ: Tilt of pendulum housing

$\dot{\phi}$: Angular velocity of pendulum

$\ddot{\phi}$: Angular acceleration of pendulum

R_i: Outside radius of inner cylinder

R_o: Inside radius of outer cylinder

V: Relative squeeze velocity of damper drums

Y: $\frac{y}{\ell}$

y: Distance from bottom of the damper to the top of the damper

ζ: Damping factor

ABSTRACT

A mechanism is proposed as a means of passively leveling an optical assembly about two horizontal axes within a tolerance of one arc-second. The mechanism is designed so that it will stimulate a spherical pendulum for input motions up to 100 arc-seconds. In order to insure the operation of the mechanism and establish the proper geometry, three analytical models were developed. Planar and spatial models which assumed rigid links with pin joints and a planar model assuming deformable links with pin and clamped joints were studied. These results are compared with experimental data gathered for three geometry combinations.

It is shown that the results from the planar and spatial analytics agree to within 10%, with the spatial model predicting less error. Hence, the less complicated planar analysis may be performed with little loss in accuracy. Neither rigid link models compare well with the experimental data, with as much as an 80% discrepancy in some cases. When deformable links are included in the planar model, the results are within 16% of the experimental results. This indicates that the resistance to bending at the points can not be neglected in modeling the mechanism. The mechanism to act like a spherical pendulum, and guidelines are established for the design.

CHAPTER 1

INTRODUCTION

1.1 Machine Error Detection from an Absolute Reference

The impetus for this work has been the development of a two-axis monitor for use as a means of identifying thermal distortion and positioning errors in a medium accuracy CNC horizontal milling machine, while operating in a production environment.

In an effort to calibrate the machine at regular intervals of one to two hours and in as short a time as possible, a specialized and dependable instrument is needed. Standard instruments such as interferometers, electronic levels and touch probes are disadvantageous because either too little information can be obtained in a short time, or inordinate set up times are required.

At this junction, an optical system was proposed which would serve to indicate work-space distortion, in the form of rotations about an absolute axis to an accuracy of 1 arc second.

Fig 1.1a depicts the elements of this concept. The pallet carries a 4 x 4 x 4 matrix of detectors which are targeted by a laser. An entire row of detectors is targeted simultaneously by a horizontal thin plane of light. This plane of light is created by sending the laser beam through a vertically mounted cylindrical lens of short focal length as in Figure 1.1b. An entire column of detectors is targeted simultaneously by rotating the cylindrical lens into a horizontal position as in Fig 1.1c.

Figures 1.2 and 1.3 show the emitter system in more detail and its passive leveling suspension which is intended to hold the instrument level to within 1 arc sec.

1.2 Variables in a Precision Two Axis Level

Figure 1.2 is an idealized suspension of flexible filaments which converge to a point. Such a pendulum will produce a level platform if the C.G. is directly below the vertex of the system and if all the suspension elements are equal length and have infinite flexibility. In reality, none of these conditions is met. In the light of the error goal of θ_0 = 1 arc second, the minute deviations from the ideal geometry can have significant effects. To begin with, there is no true vertex to the suspension filaments because the wires must be at least .006 in diameter to support even the low weight of the lasers and lenses. The inset of Figure 1.2 demonstrates that instead of a vertex, the wires are

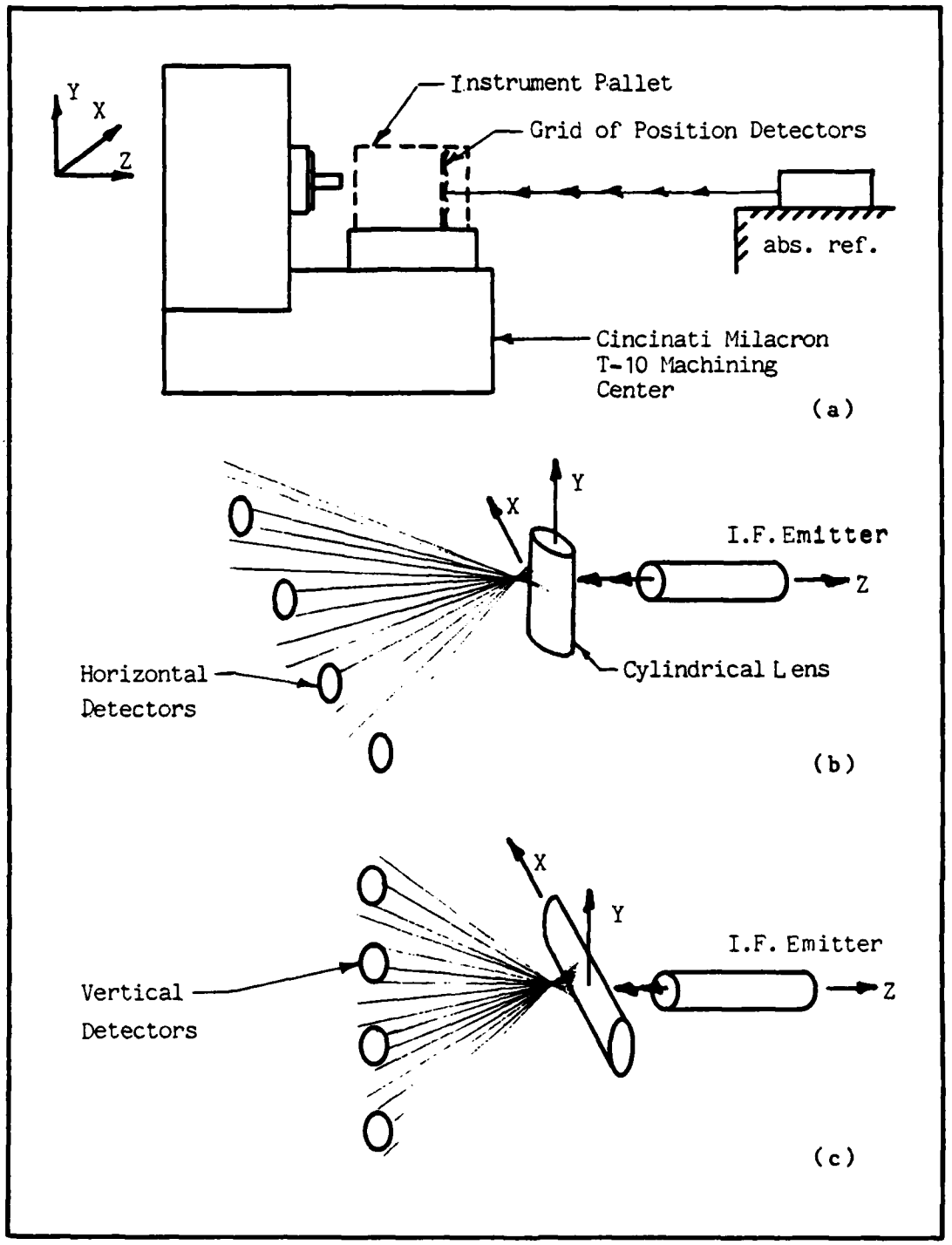

Figure 1.1 Proposed optical calibration system.

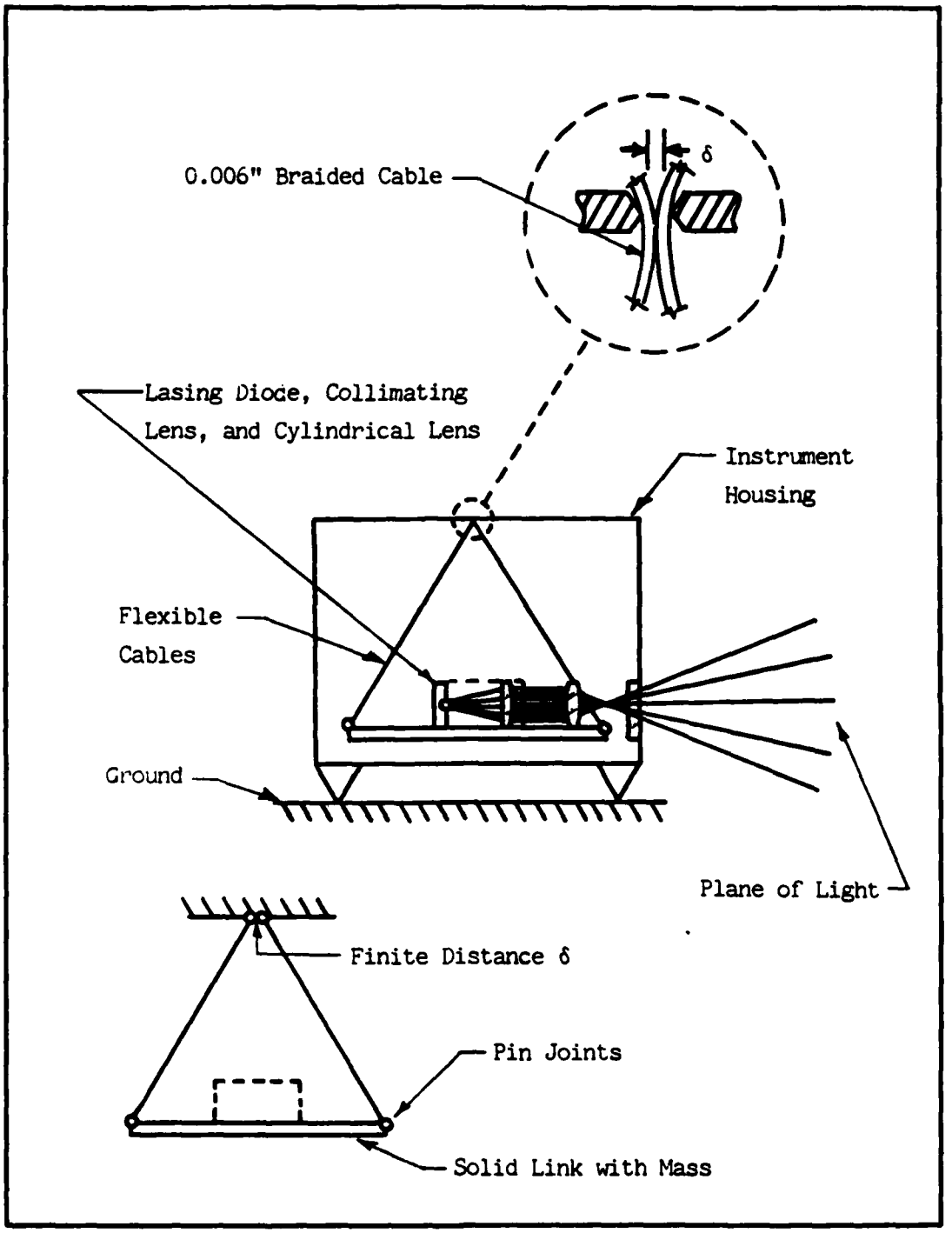

Figure 1.2 Schematic representation of the instrument indicating the kinematic association to a to a fourbar mechanism.

actually separated by a distance δ so that the suspension is of the kinematic type shown by Fig 1.3. The upper plate represents the housing of the instrument. When the housing is tipped through an angle θ_i the bottom platform will not remain level but will experience a tilt θ_0. Although θ_0 is smaller than θ_i, it could nevertheless exceed the tight objective of $\theta_0 < 1$ arc sec. The disruptive role of unequal wire lengths and tolerances in C.G. location will contribute to the errors in the instrument. The purpose of the initial research was to determine the role of these tolerances to the errors in instrument suspensions.

It is doubtful that the instrument will be mounted on a stationary surface since it will be used in a production environment. It is therefore essential to minimize any oscillations of the optics in order to maintain the tight constraints previously imposed on the system. So as not to interfere with the mechanism, the damper must be free of friction. Figure 1.4 illustrates an air damper consisting of two cylinders, the inner attached to the bottom plate of the mechanism while the outer cylinder is attached to ground. Although simple in design, oscillations in both the X and Z directions can be effectively damped. Air damping is more difficult to achieve due to the low viscosity of the air, while on the other hand, it does not require seals or submersion of the optics as would be required with oil or some other medium.

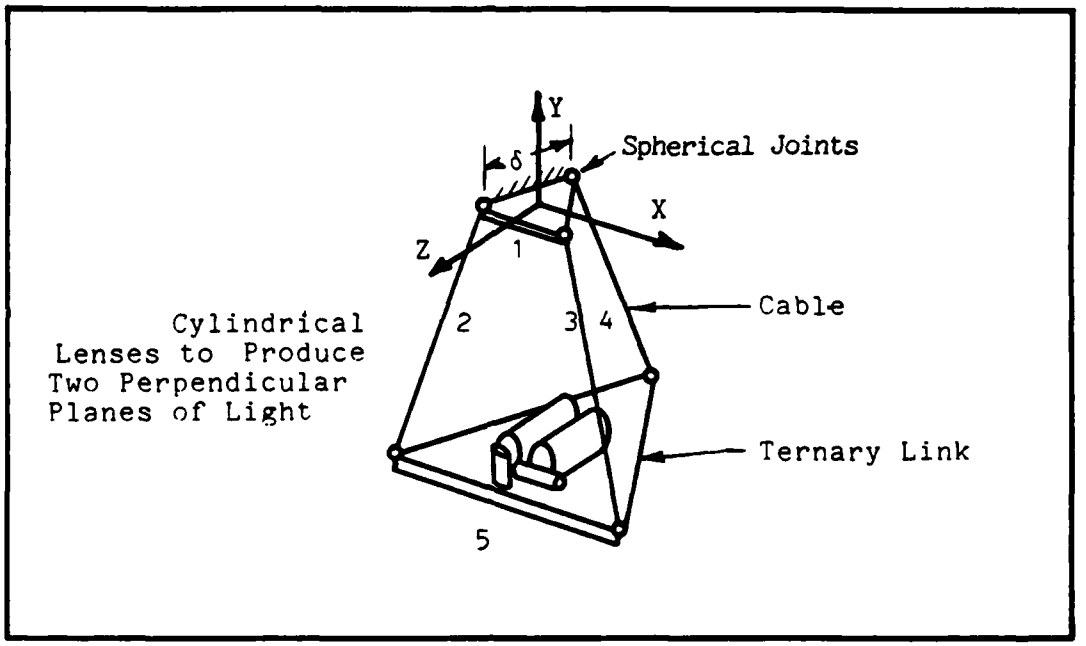

Figure 1.3 Schematic representation of the instrument indicating a 3 dimensional mechanism.

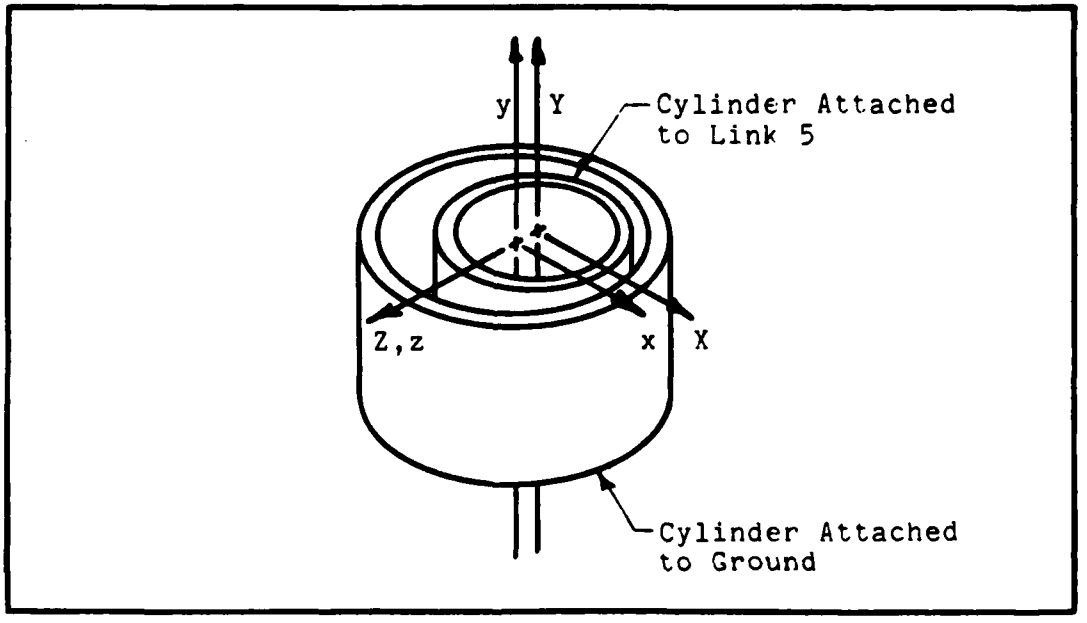

Figure 1.4 Cylindrical air damper for the two axes level.

The last section of this report focuses on the analysis and experimentation required to specify appropriate geometrical relationships to facilitate the design of such a damper.

CHAPTER 2

PLANAR ANALYSIS

2.1 Objectives

The goal of this analysis and those to follow is to determine the influence of the geometry of the mechanism on positioning errors. The positioning error is defined to be a deviation of the bottom plate from the horizontal. This angle will be represented throughout as θ_o. The results of this analysis will be used to determine the feasibility of this type of mechanism to remain level and the geometric constraints which must be satisfied in order to minimize θ_o.

2.2 Development of Equations

The mechanism under investigation is a 3 dimensional linkage. However, the problem will be addressed initially by reducing the general case to 2 dimensions. The simpler case offers expedient insight into the significant parameters of the system, which for this analysis will be the lengths of the input link (δ) and output link (L), height of the mechanism (h), the centering of the optics (Δ) and the distance that the optics lie in a vertical plane from the

output link (ε). The 2 dimensional mechanism is shown in Figure 2.1.

The assumptions used in this analysis are:

* The cables are infinitly flexible
* Frictionless pin joints
* Constant link lengths
* Links 2 & 4 are two force members.

The model is reduced to a four-bar linkage with the input rotation being link 1, as shown in Figure 2.2. A mass is fixed to link 3 at some known location, G, relative to pin joint A. The kinematics of the linkage can be written as.

$$(\ell_{AC})^2 = (Ax-Cx)^2 + (Ay-Cy)^2 \qquad (2.1)$$

$$(\ell_{BD})^2 = (Bx-Dx)^2 + (By-Dy)^2 \qquad (2.2)$$

$$(\ell_{DC})^2 = (Dx-Cx)^2 + (Dy-Cy)^2 \qquad (2.3)$$

The location of the center of gravity is fixed by link 5.

$$(\ell_{GC})^2 = (Gx-Cx)^2 + (Gy-Cy)^2 \qquad (2.4)$$

$$(\ell_{GD})^2 = (Gx-Dx)^2 + (Gy-Dy)^2 \qquad (2.5)$$

Referring to Figure 2.2, for static equilibrium the forces and moments on link 3 are conserved which yields:

$$\Sigma F_3 = 0$$

$$f_{AC}\bar{e}_{A/C} + f_{BD}\bar{e}_{B/D} - mg\bar{j} = 0 \qquad (2.6)$$

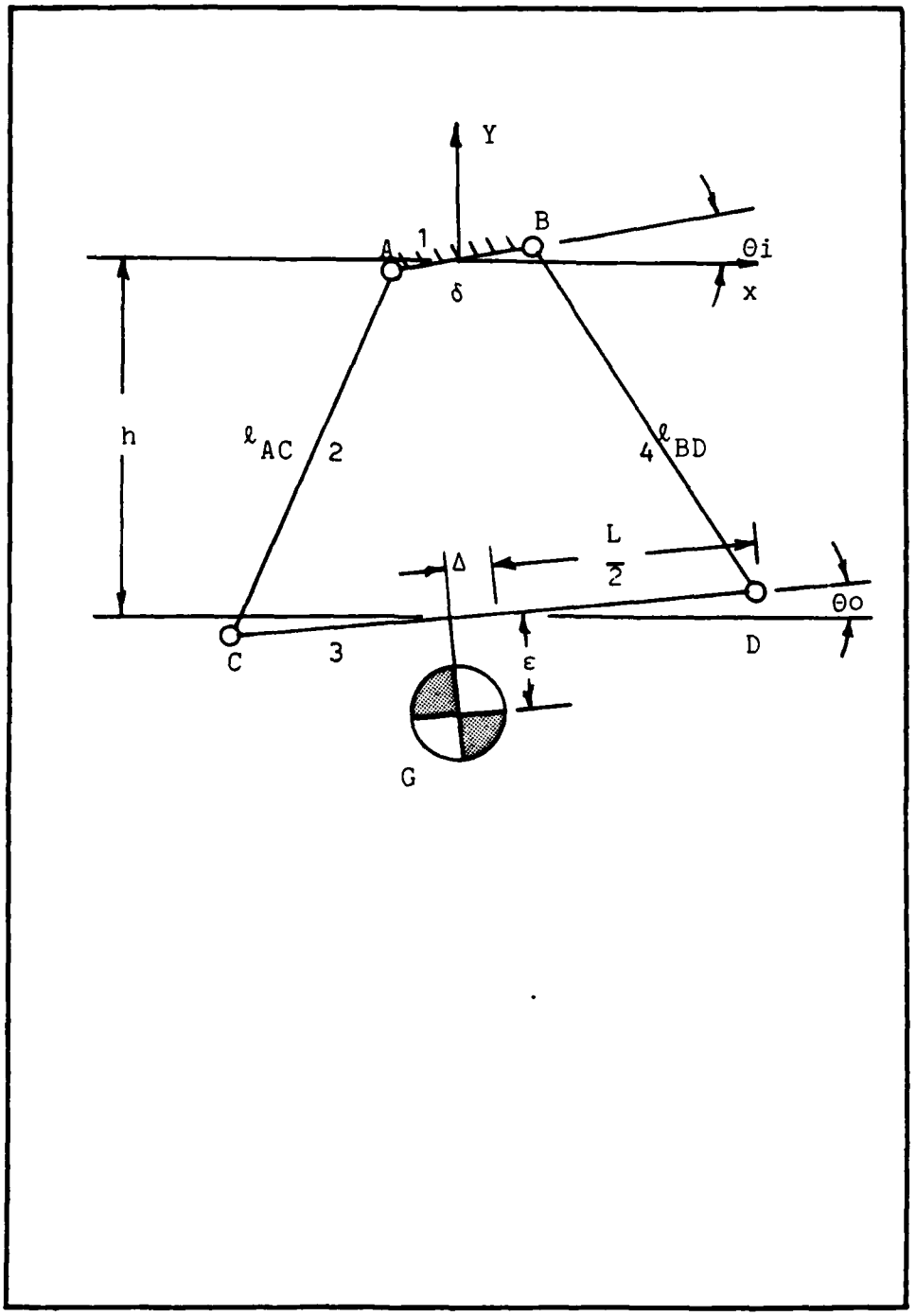

Figure 2.1 Illustration of the variables for the planar kinematic analysis.

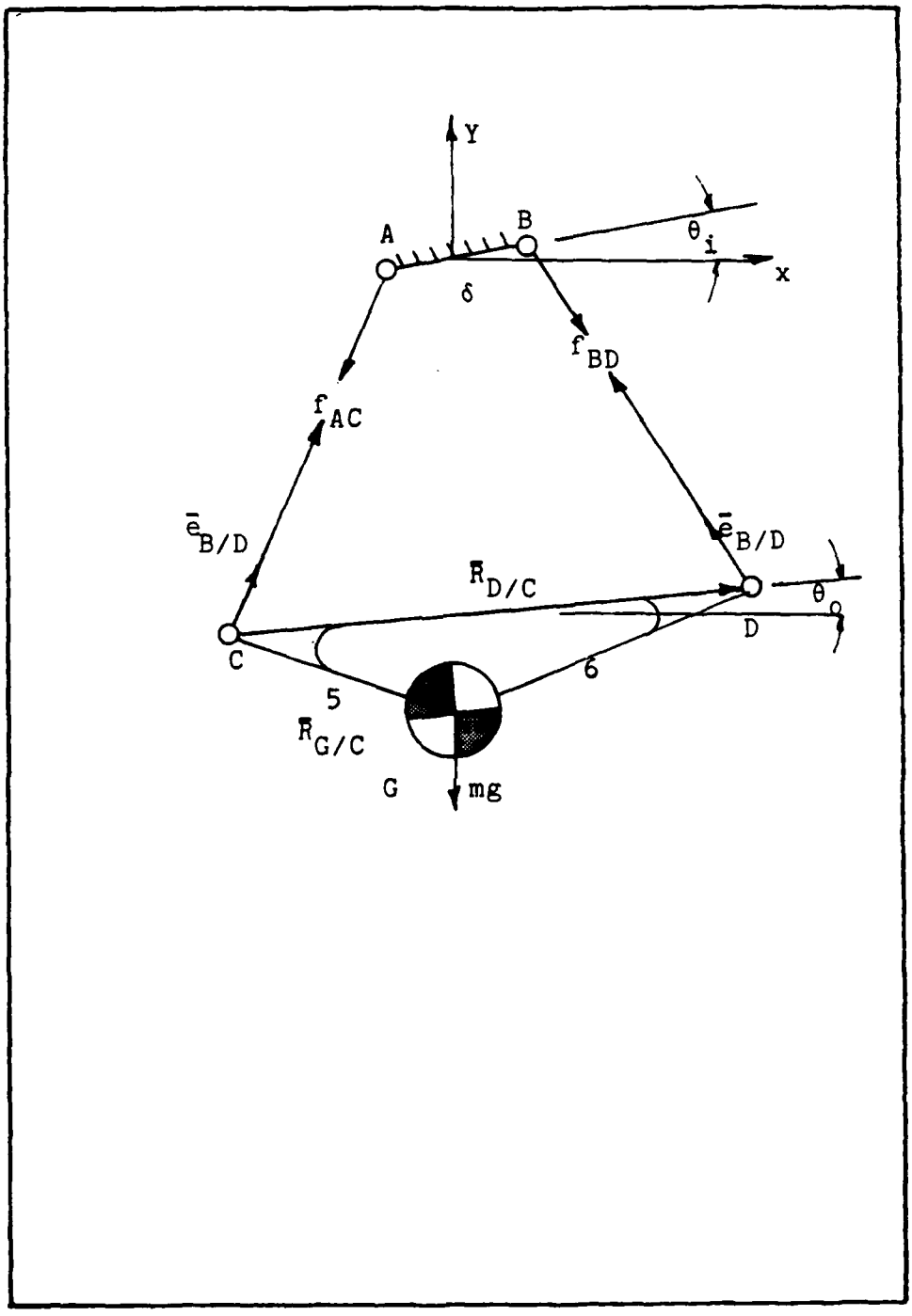

Figure 2.2 Illustration of the forces and moments acting on the output link.

$$\Sigma M_C = 0$$

$$\bar{R}_{D/C} \times f_{BD}\bar{e}_{B/D} - \bar{R}_{G/C} \times mg\bar{j} = 0 \qquad (2.7)$$

Where,

$$\bar{e}_{A/C} = \frac{(Ax-Cx)}{\ell_{AC}}\bar{i} + \frac{(Ay-Cy)}{\ell_{AC}}\bar{j}$$

$$\bar{e}_{B/D} = \frac{(Bx-Dx)}{\ell_{BD}}\bar{i} + \frac{(By-Dy)}{\ell_{BD}}\bar{j}$$

$$\bar{e}_{G/C} = \frac{(Gx-Cx)}{\ell_{GC}}\bar{i} + \frac{(Gy-Cy)}{\ell_{GC}}\bar{j}$$

Insertion of the unit vectors into Equation 2.6 yields:

$$\frac{f_{AC}}{\ell_{AC}}(Ax-Cx) + \frac{f_{BD}}{\ell_{BD}}(Bx-Dx) = 0 \quad :\bar{i} \qquad (2.8)$$

$$\frac{f_{AC}}{\ell_{AC}}(Ay-Cy) + \frac{f_{BD}}{\ell_{BD}}(By-Dy) - mg = 0 \quad :\bar{j} \qquad (2.9)$$

and Equation 2.7 becomes:

$$\frac{f_{BD}}{\ell_{BD}}\Big\{(Dx-Cx)(By-Dy)-(Dy-Cy)(Bx-Dx)\Big\} - mg(Gx-Cx) = 0 \qquad (2.10)$$

Equations 2.1 - 2.5 and 2.8 - 2.10 describe the eight unknowns for the position solution of link 3 (given the points A, B and the geometry, links 1, 2, 3 and 4). The solution was carried out by solving the eight non-linear equations for points C,D and G numerically using a Newton-Rapson Method.

The ouput angle θ_o can then be found from the tangent of points D and C.

2.3 Results from Planar Analysis

In order to generalize the results, the geometry will be described as ratios of link 3 or "L". This analysis showed that for small angles, the input (θ_i) output (θ_o) relationship was linear as would be expected for small motions. The ratio of $\frac{\theta_o}{\theta_i}$ has been labeled K and is the measure of the performance of the mechanism.

The K ratio is plotted against the $\frac{\delta}{L}$ ratio in Figure 2.3 for several cases of $\frac{h}{L}$. As can be seen, K goes to zero only when the input link, (δ), goes to zero (a true pendulum) or the height h goes to infinity (the effect of δ is lessened). But there is a physical limitation of the size of both δ and h. The construction of the top link forces δ to be at least one wire diameter. (See insert on Figure 1.2) Therefore, the only way to decrease $\frac{\delta}{L}$ is to increase the length of the output link. For packaging purposes, it is desirable to minimize the height of the mechanism. From Figure 2.3, it is therefore advisable to generate a mechanism which has an $\frac{h}{L}$ ratio about unity since $\frac{h}{L}$ much greater than unity offers little improvement on K.

The effect of $\frac{\Delta}{L}$ is illustrated in Figure 2.4, where it can be seen that $\frac{\Delta}{L}$ may vary up 50% without introducing posi-

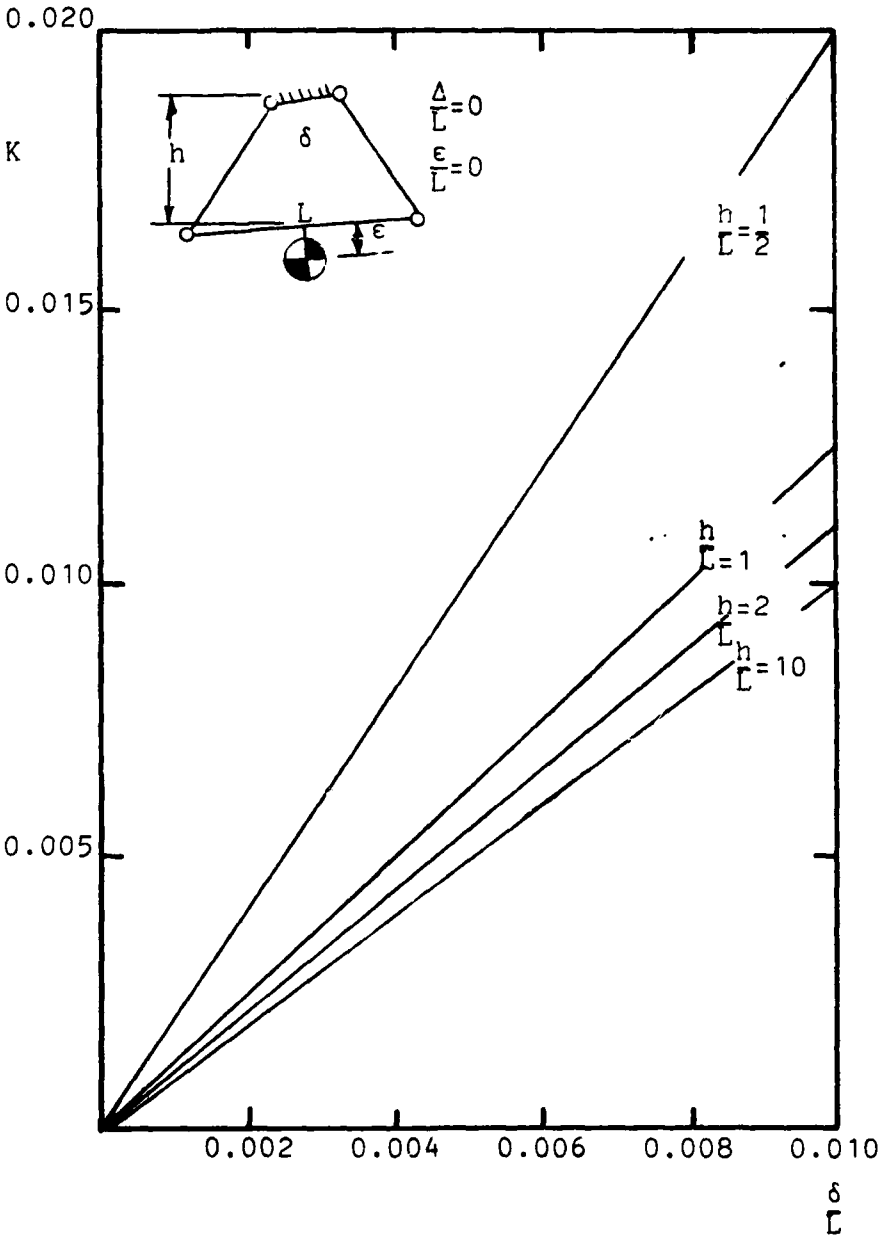

Figure 2.3 K vs δ/L as a function of h/L from the planar analysis.

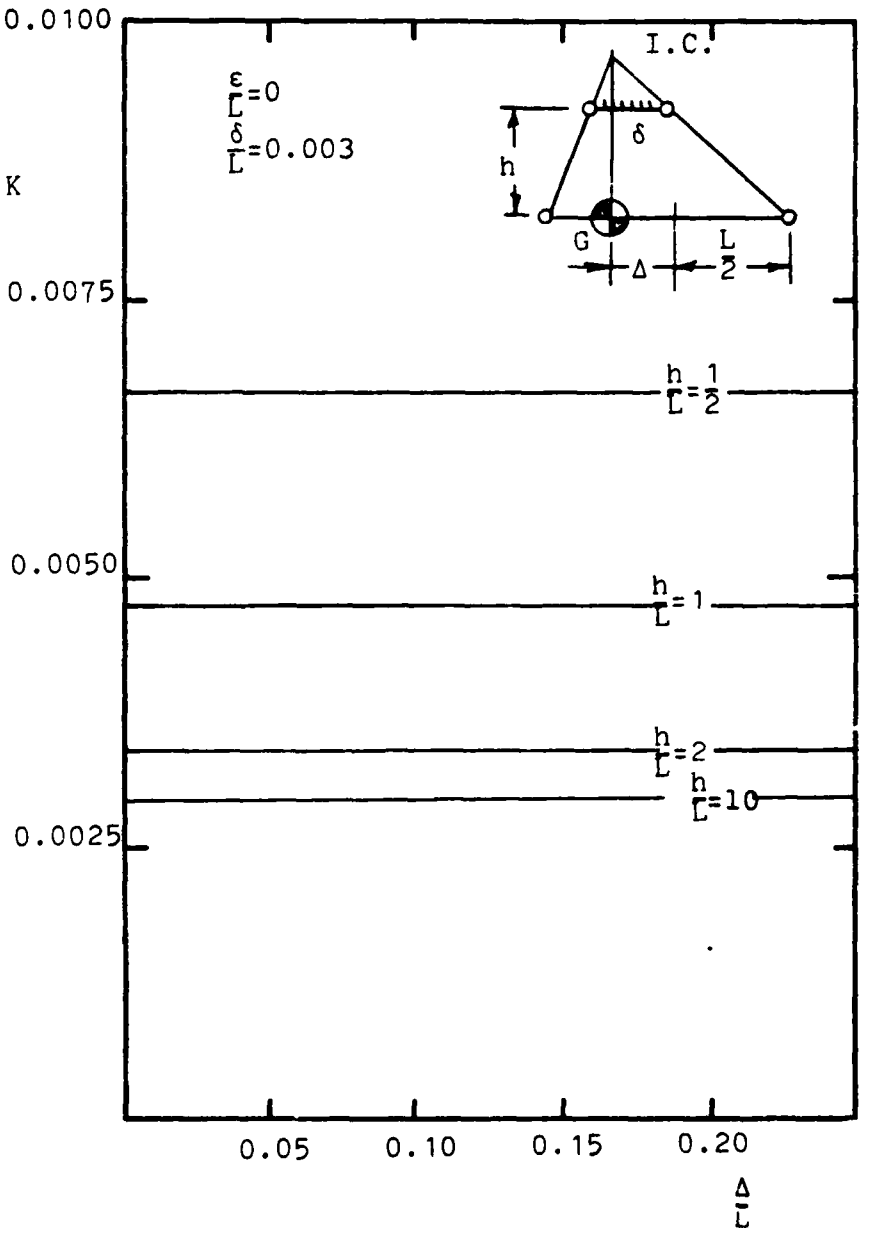

Figure 2.4 K vs ε/L as a function of h/L from the planar analysis.

tioning errors. At first this result seemed spurious, but a look at the configuration of the mechanism with $\theta_o = 0$ explains the results. The inset of Figure 2.4 shows that during assembly the instant center of link 1 with respect to link 3 is brought to a point directly above the mass center of the mechanism, while the wire lengths are altered such that the bottom link is horizontal. By a simple trigonometric analysis, it can be shown that this assembly procedure causes the distance from the center of mass to the instant center to be independent of Δ. (The distance between links 1 and 3 is fixed by h.)

Since the angular velocity ratio for any two links in a mechanism is inversely proportional to the distances from the instant centers in the frame about which the links are rotating to the instant center which is common to the two links, the assembly procedure fixes the velocity ratio. The angular velocity ratio is simply K since the relative rotations are small in this mechanism. Thus, K remains unaltered because the distances from the instant center to links 1 and 3 are independent of Δ and therefore fixing the velocity ratio, K, by this constant distance ratio.

The effect of $\frac{\varepsilon}{L}$ on K is shown in Figure 2.5. It is important to note that the mass center should lie below the bottom link, since K increases as the output link length ε

decreases. With a negative value of ε, K increases monotonically, whereas a large positive value for ε significantly reduces K. Since the value of $\frac{\varepsilon}{L}$ is a design choice, it is recommended to make this value as large as possible.

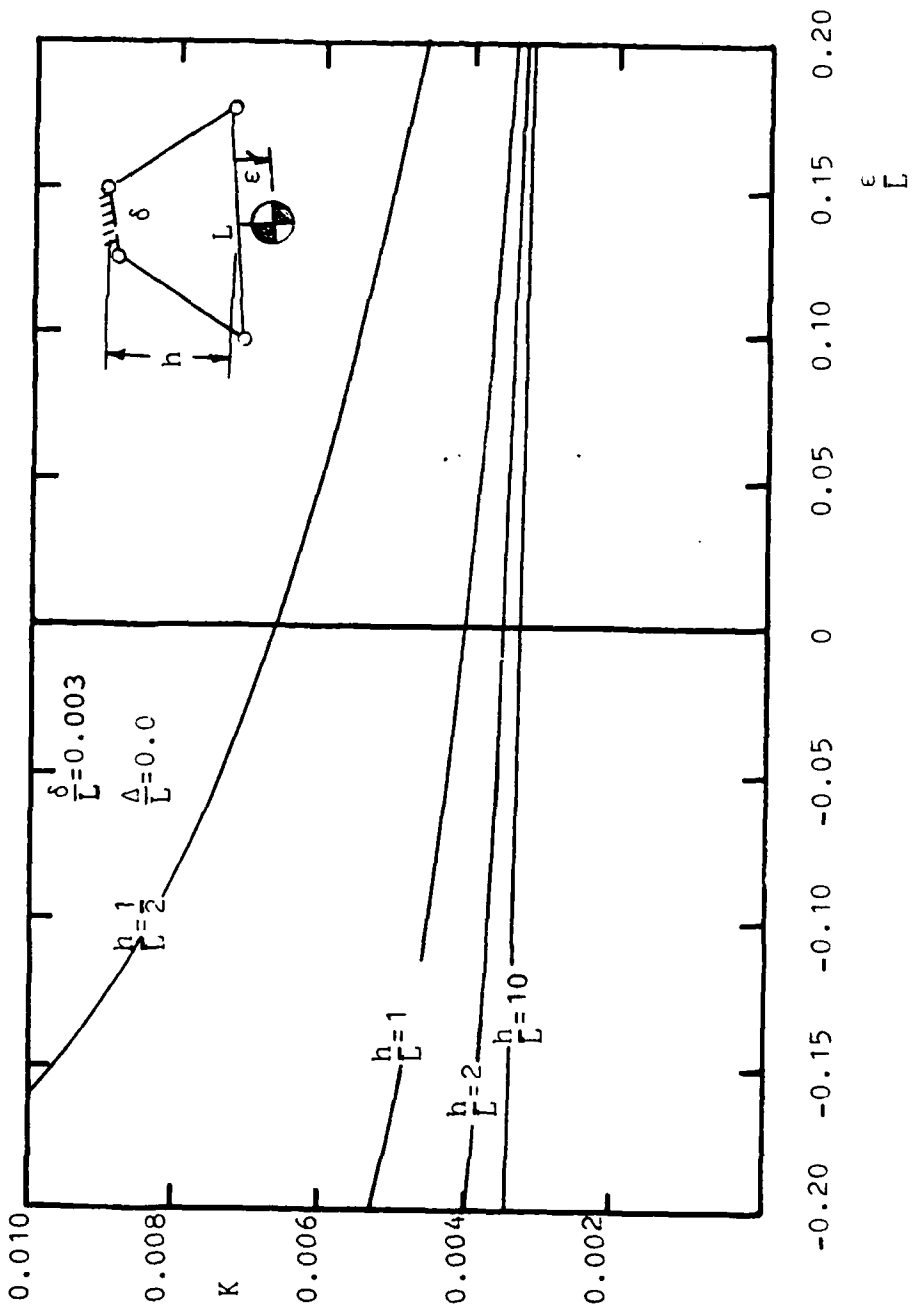

Figure 2.5 K vs Δ/L as a function of h/L from the planar analysis.

CHAPTER 3

SPATIAL ANALYSIS

3.1 Objectives

While the 2 dimensional analysis is a good indicator of the influence of the geometry on the output θ_o, a 3 dimensional analysis will show the rotations out of the plane of the 2 dimensional mechanism. In this section we will focus on the static equilibrium position of the mechanism in 3 dimensions subject to input rotations (θ_i) about the X and Z axis as illustrated in Figure 3.1. The results will then be compared to the results from the previous section in order to understand the validity of the two-dimensional analysis.

3.2 Development of Equations

Multiple starts were made to this problem in order to find an approach with sufficient accuracy to indicate rotations on the order of arc seconds, while simultaneously holding the computational time to a minimum. The first attempt was to use IMP [1], a general purpose mechanism analysis computer program, but the solution was too coarse

[1] Sheth, P.N. and Vicker, J.J. Jr., "IMP (Integrated

to be of any value. The vector loop approach produces coupled, transcendental equations. While this creates no difficulties in planar analysis, standard numerical techniques experience difficulties in converging on a solution to the large number of equations required for spatial analysis. The situation does not change when small rotations are assumed about the equilibrium position because the equations remain linearly coupled by cross products. Since the variables are small, again convergence problems arise in numerical equation solvers.

Minimization of potential energy was explored as an alternative means of developing the equations of motion. The creation of multiple partial differentials which could not be determined algebraically forced the use of Lagrange Multipliers to evaluate the partials. When the Lagrange Multipliers are coupled with the constraint equations, the number of equations is increased to 30.

The final approach contained herein is less elegant in nature but requires significantly fewer constraint equations (15). These equations are still non-linear, but the equation solver converges rapidly because the variables, the coordinates of the spherical joints, are relatively large.

Mechanisms Program), A Computer-Aided Design Analysis System for Mechanisms and Linkages", Journal Engineering for Industry, Trans. ASME, Ser. B, Vol. 99, no. 3, August 1977, pp. 773-778.

This approach to the spatial analysis is basically the same as the planar analysis, except it allows motion in three directions; that is, the mass of the optics is at some point G on the ternary output link (as shown in Figure 3.1) and the link lengths are constant with frictionless spherical joints. The input rotation is about the X and Z axis located at the center of the input link. Rotation of the input link about the Y axis does not alter the magnitude of the output, in that it merely rotates the coordinate system. The analysis is predicated on knowing the initial coordinates of points A, B and C. Following any input (θ_i), the resulting coordinates of A,B and C are calculated via a rotation matrix.

The first equations of constraint are those of constant link lengths, Figure 3.1.

$$(\ell_{DF})^2 = (Dx-Fx)^2+(Dy-Fy)^2+(Dz-Fz)^2 \qquad (3.1)$$

$$(\ell_{DE})^2 = (Dx-Ex)^2+(Dy-Ey)^2+(Dz-Ez)^2 \qquad (3.2)$$

$$(\ell_{EF})^2 = (Ex-Fx)^2+(Ey-Fy)^2+(Ez-Fz)^2 \qquad (3.3)$$

$$(\ell_{AD})^2 = (Ax-Dx)^2+(Ay-Dy)^2+(Az-Dz)^2 \qquad (3.4)$$

$$(\ell_{BE})^2 = (Bx-Ex)^2+(By-Ey)^2+(Bz-Ez)^2 \qquad (3.5)$$

$$(\ell_{CF})^2 = (Cx-Fx)^2+(Cy-Fy)^2+(Cz-Fz)^2 \qquad (3.6)$$

$$(\ell_{GD})^2 = (Gx-Dx)^2+(Gy-Dy)^2+(Gz-Dz)^2 \qquad (3.7)$$

$$(\ell_{GE})^2 = (Gx-Ex)^2+(Gy-Ey)^2+(Gz-Ez)^2 \qquad (3.8)$$

$$(\ell_{GF})^2 = (Gx-Fx)^2+(Gy-Fy)^2+(Gz-Fz)^2 \qquad (3.9)$$

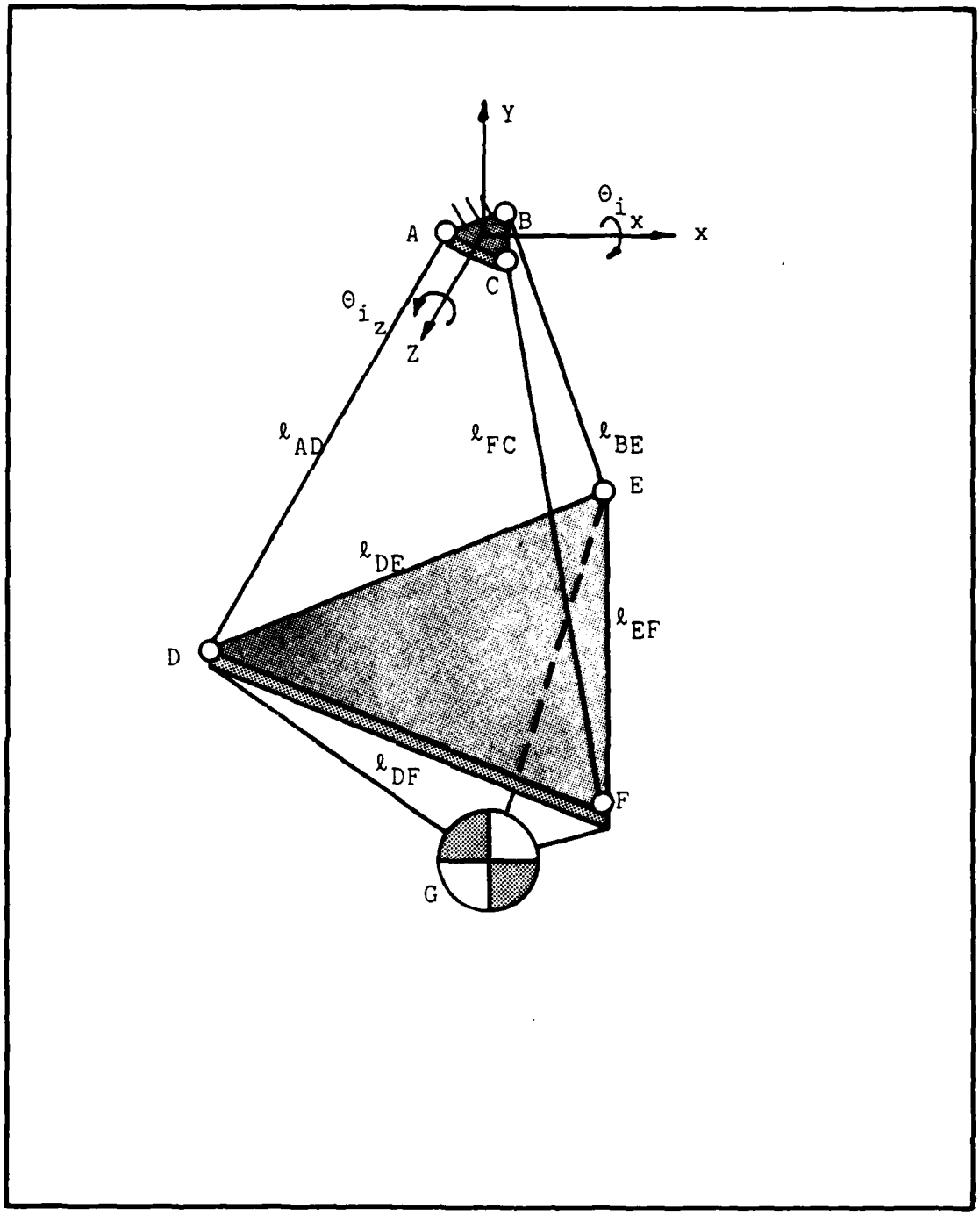

Figure 3.1 Illustration of the variables for the spatial kinematic analysis.

For static equilibrium, Figure 3.2.

$$\Sigma F_5 = 0$$

$$f_{AD}\bar{e}_{A/D} + f_{BE}\bar{e}_{B/E} + f_{CF}\bar{e}_{C/F} = mg\bar{j} \qquad (3.10)$$

$$\Sigma M_G = 0$$

$$\bar{R}_{D/G} \times f_{AD}\bar{e}_{A/D} + \bar{R}_{E/G} \times f_{BE}\bar{e}_{B/E} + \bar{R}_{F/G} \times f_{CF}\bar{e}_{C/F} = 0 \qquad (3.11)$$

When the unit vectors are introduced into Equation 3.10 and the multiplications carried out, these equations become:

$$\frac{f_{AD}}{\ell_{AD}}(Ax-Dx)+\frac{f_{BE}}{\ell_{BE}}(Bx-Ex)+\frac{f_{CF}}{\ell_{CF}}(Cx-Fx) = 0 \quad :\bar{i} \qquad (3.12)$$

$$\frac{f_{AD}}{\ell_{AD}}(Ay-Dy)+\frac{f_{BE}}{\ell_{BE}}(By-Ey)+\frac{f_{CF}}{\ell_{CF}}(Cy-Fy) = mg \quad :\bar{j} \qquad (3.13)$$

$$\frac{f_{AD}}{\ell_{AD}}(Az-Dz)+\frac{f_{BE}}{\ell_{BE}}(Bz-Ez)+\frac{f_{CF}}{\ell_{CF}}(Cz-Fz) = 0 \quad :\bar{k} \qquad (3.14)$$

Taking the cross products in Equation 3.11 yields the following:

$$\frac{f_{AD}}{\ell_{AD}}\{(Dy-Gy)(Az-Dz) - (Dz-Gz)(Ay-Dy)\} + \frac{f_{BE}}{\ell_{BE}}\{(Ey-Gy)(Bz-Ez) - (Ez-Gz)(By-Ey)\} + \frac{f_{CF}}{\ell_{CF}}\{(Fy-Gy)(Cz-Fz) - (Fz-Gz)(Cy-Fy)\} = 0 \quad :\bar{i} \qquad (3.15)$$

$$\frac{f_{AD}}{\ell_{AD}}\{(Dz-Gz)(Ax-Dx) - (Dx-Gx)(Az-Dz)\} + \frac{f_{BE}}{\ell_{BE}}\{(Ez-Gz)(Bx-Ex) - (Ex-Gx)(Bz-Ez)\} + \frac{f_{CF}}{\ell_{CF}}\{(Fz-Gz)(Cx-Fx) - (Fx-Gx)(Cz-Fz)\} = 0 \quad :\bar{j} \qquad (3.16)$$

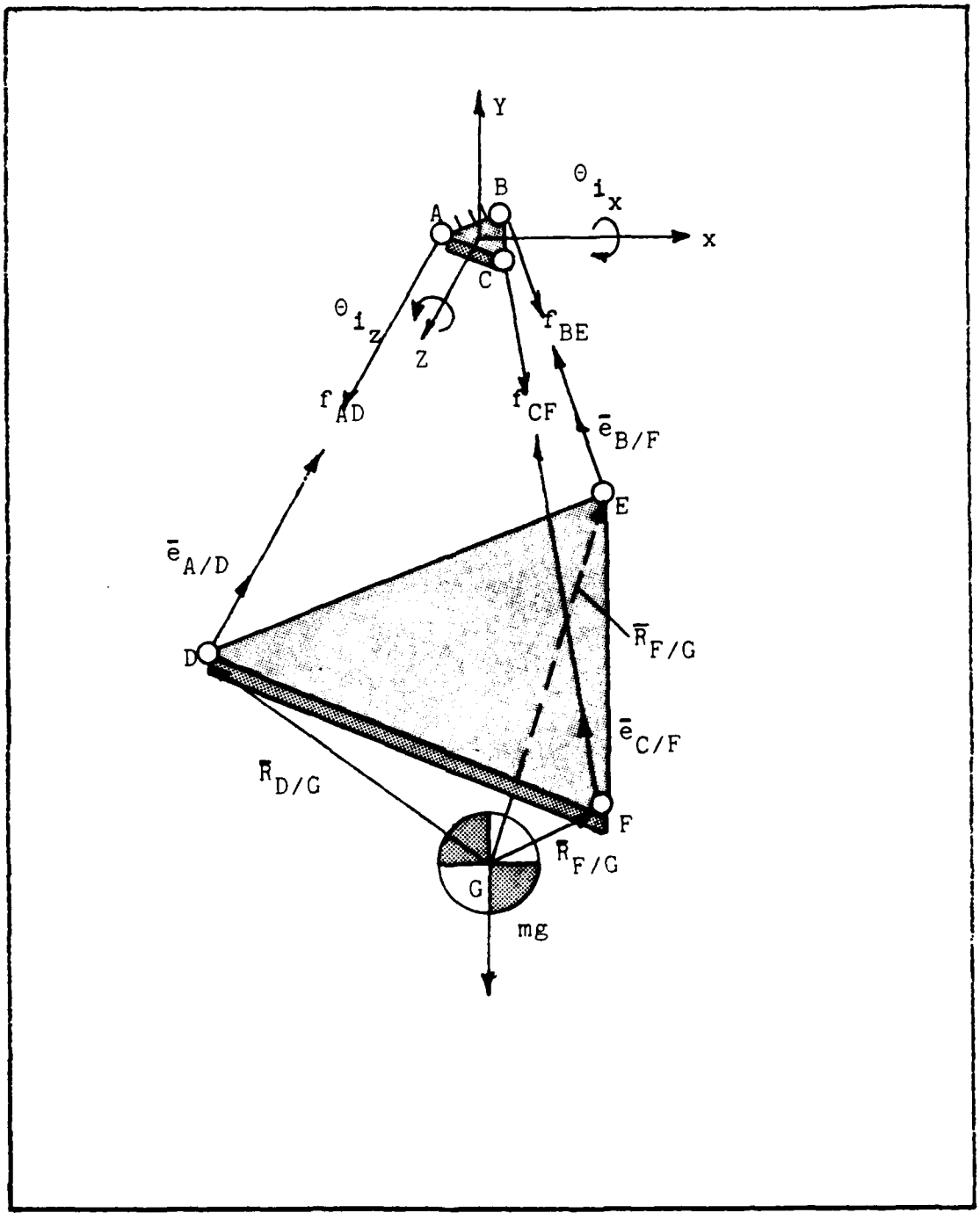

Figure 3.2 Illustration of the forces and moments acting on the output link.

$$\frac{t_{AD}}{\ell_{AD}}\{(Dx-Gx)(Ay-Dy) - (Dy-Gy)(Ax-Dx)\}$$

$$+ \frac{t_{BE}}{\ell_{BE}}\{(Ex-Gx)(By-Gy) - (Ey-Gy)(Bx-Ex)\}$$

$$+ \frac{t_{CF}}{\ell_{CF}}\{(Fx-Gx)(Cy-Fy) - (Fy-Gy)(Cx-Fx)\} = 0 \quad :\bar{k} \qquad (3.17)$$

Equations 3.1-3.9 and 3.12-3.17 are then solved numerically for the coordinates of points D, E and F on the output link. The output rotations are then calculated using Rodrigues' formula [2] to find the rotation of the normal to the output link from the initial assembly position. Rodrigues' formula is used rather than a general displacement matrix to reduce computational time.

3.3 Comparison of the Spatial and Planar Results

First, Rodrigues' formula is only valid when a body is rotating about a fixed axis without any translations. This was verified by calculating the displacements of the output link using a general displacement matrix, and then noting that the displacement terms were equal to zero.

The primary results of this analysis are displayed in Figure 3.3, where K' is plotted against $\frac{\delta}{L}$ for different values of $\frac{h}{L}$. The ratio K' is the magnitude of the rotation of the output link about the X and Z axes over the magnitude of the input rotation. The 3 dimensional analysis of the

[2] Bisshopp, K.E., "Finite Rotations of a Rigid Body and the Airplane Landing Gear Problem", Jnl. Mechanisms, Vol. 3, Pergamon Press, 1968, pp.203-208.

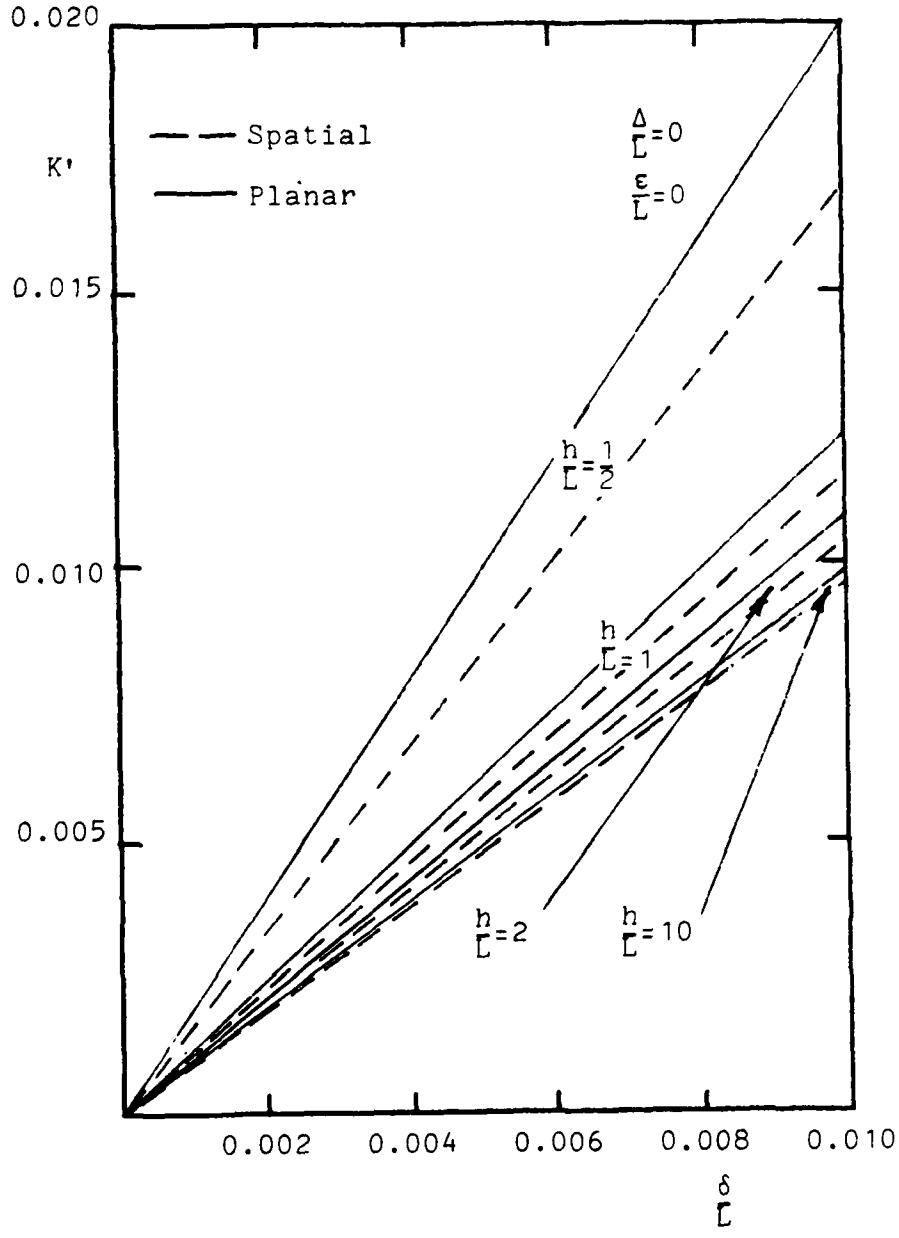

Figure 3.3 K´ vs δ/L as a function of h/L from the spatial analysis with comparisons to the planar analysis.

mechanism indicates a smaller K than that predicted by the 2 dimensional analysis due to rotations on the order of hundreds of arc-seconds of the output link about the Y axis.

Figure 3.4 illustrates K′ verses $\frac{\varepsilon}{L}$, for various $\frac{h}{L}$ ratios, and a comparison with Figure 2.5. As previously shown in Figure 3.3, the spatial analysis yields a lower K than does the planar. It can be seen that the difference between the spatial and planar, at each $\frac{h}{L}$, is similar to that seen in Figure 3.3, and that the curves for the spatial and planar models begin to coalesce as $\frac{h}{L}$ or $\frac{\varepsilon}{L}$ go to infinity.

Since the two models predict the same performance as $\frac{\delta}{L}$ goes to zero or $\frac{h}{L}$ goes to infinity, we can conclude that the planar analysis is a suitable substitute for the spatial model, with the understanding that K found from the planar is larger than K′ found from the spatial analysis.

Figure 3.5 illustrates the change in one of the output link lengths, while the two others are held equal. The figure shows that K′ actually decreases below the nominal value, all lengths (L) equal, as one length is increased to roughly 1% larger than the others. Let the input rotation be about the axis, illustrated in the inset of Figure 3.5, which is measured from the positive X axis parallel to the link which is changing, described by the angle α. The lower curve, for which the change in K′ is very severe, is the

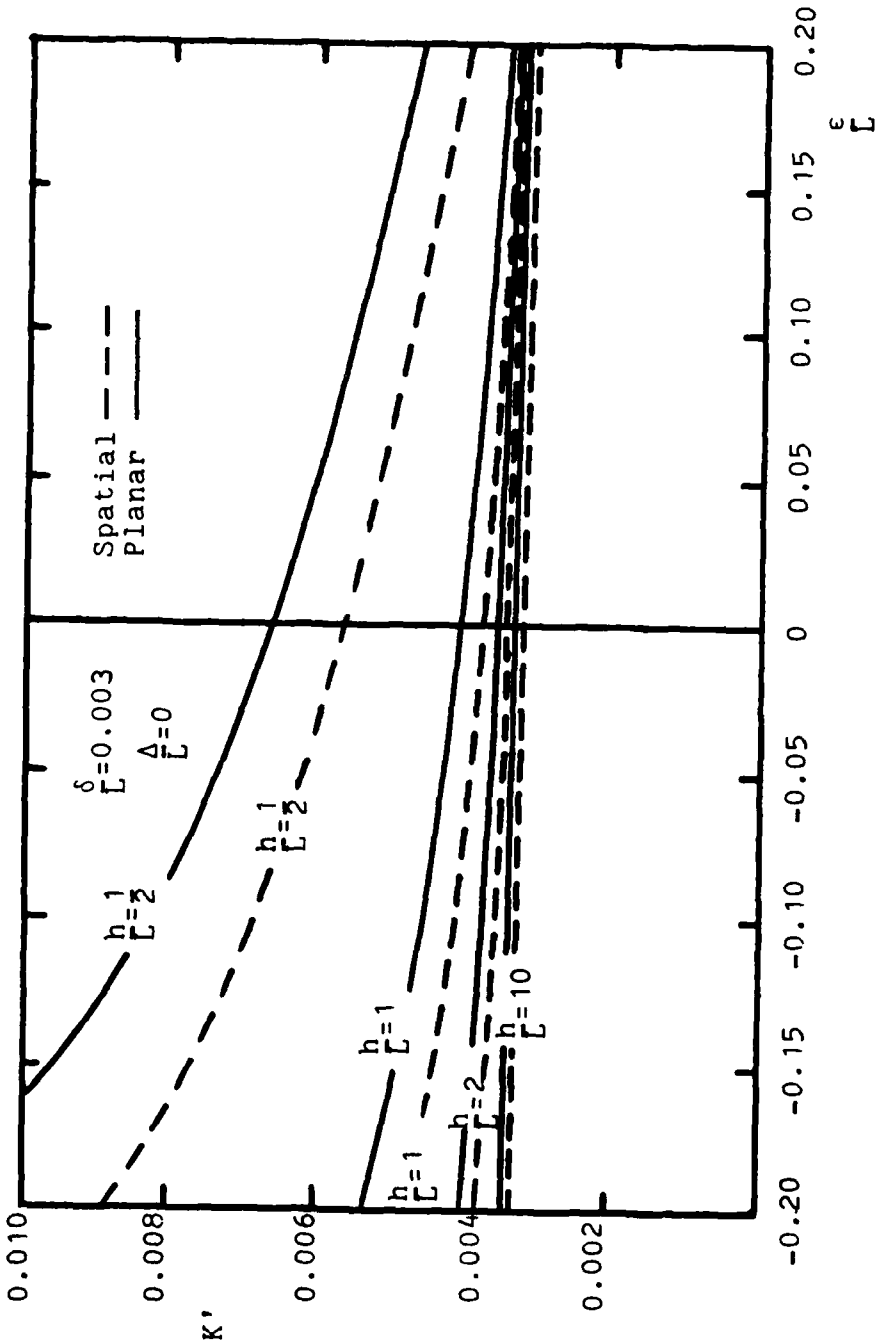

Figure 3.4 K′ vs ε/L as a function of h/L for the spatial analysis with comparisons to the planar analysis.

input rotation at α = 90 degrees from the length that has been changed. When the rotation is parallel to the length, α = 0 degrees, the minimum is the nominal value.

By looking down the α = 0 degree axis in Figure 3.5, one can see that the apparent link lengths are not altered by the change in length, and the mechanism performs as though no change had been made. On the other hand, looking down the 90 degree axis, one sees the full effect of the change in length, and hence a decrease in K'. The minimum value of K', at $\frac{\Delta L}{L}$ = 1%, is less than K' if all links are increased by 1%. This perhaps could be advantageous if the mechanism was used to level the optics about only one axis.

The results of the spatial analysis are very similar to those of the planar analysis. The planar analysis is much shorter, and the results equally as informative as the spatial analysis. The effects of one link length changing shows that K' decreases below the nominal minimum.

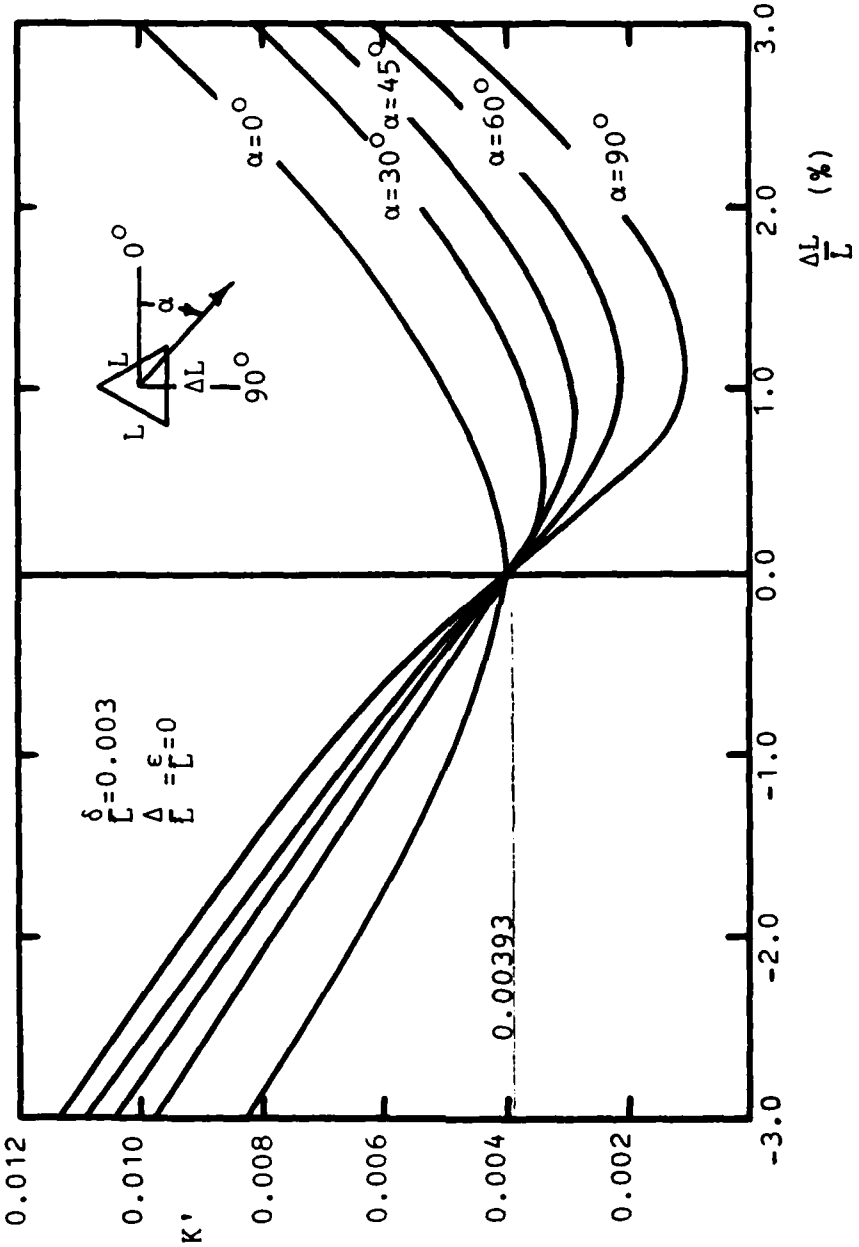

Figure 3.5 K' vs ΔL/L on the output link of the spatial mechanism.

CHAPTER 4

PLANAR MODEL ACCOUNTING FOR WIRE STIFFNESS

4.1 Objectives

As previously mentioned, links 2 & 4 are made of cable with less than ideal joints at the ends. They have been assumed to have infinite flexibility so that the bending in the cables occurs at an infinitesimal area at the the connection to the plates.

For this section the cables will have some finite stiffness and are subjected to shearing forces and moments applied to the ends. A planar model of the mechanism is developed here which includes the stiffness in the cables as a system parameter. It will be shown that including this effect in the kinematic representation of the mechanism leads to results which will agree well with the experimental data gathered in the next section.

4.2 Development of Equations

The following assumptions have been made:

* Negligible strain energy is stored in the cables at the assembly position.

* The cables are Euler-Bernoulli beams such that the curvature is proportional to the bending moment.

* Deflection of the beams is small such that bending does not alter the length of the cables.

* Strains in the individual wires of the cable are small and the axial and bending responses are additive.

* Friction and twisting in the cables are neglected.

4.2.1 Force and position solution

Upon assembly of the mechanism, the cables are plastically deformed around the junction at the input link and subsequently assume an unstressed kinked shape at this point if disassembled. The assumption of no initial stored strain energy is then an approximation to the state of the cables at assembly. This assumption will lead to a pinned boundary condition at the input link whereas a clamped boundary condition will be used at the output link. The cables will be constrained to make small deflections about the assembly position in order to simplify the analysis. These assumptions lead to a schematic representation of the mechanism as illustrated in Figure 4.1.

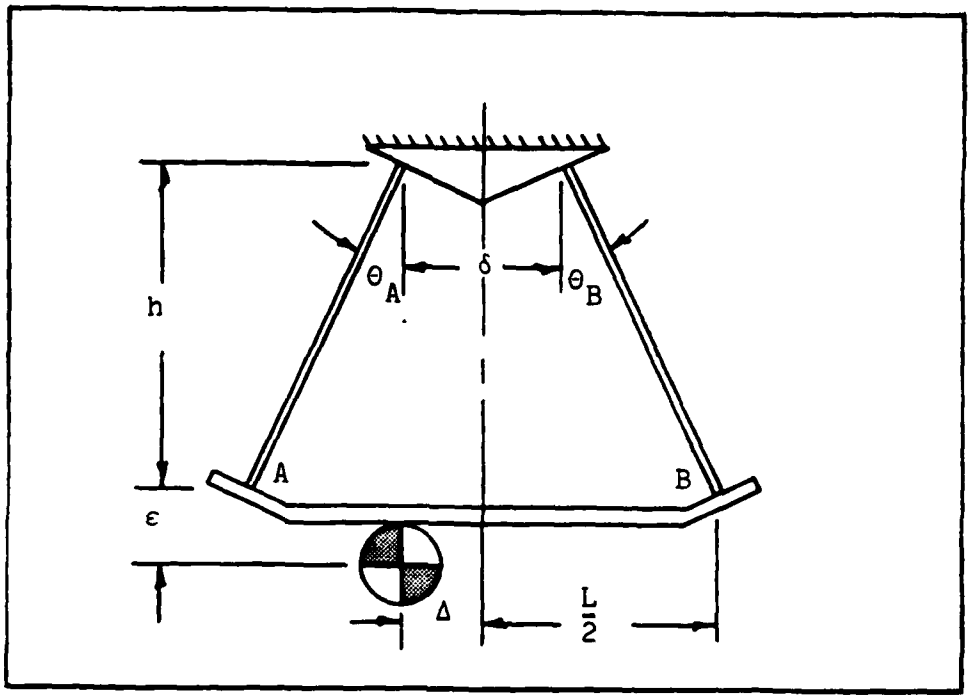

Figure 4.1 Schematic representation of the instrument produced by the assumptions of Section 4.2.

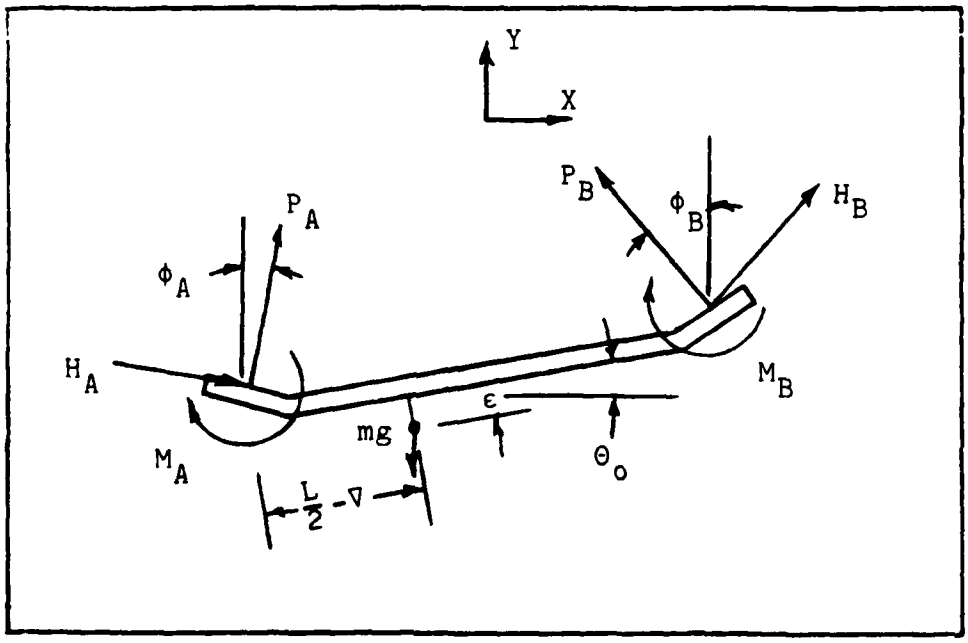

Figure 4.2 Diagram of moments and forces acting on the output link.

Let θ_A and θ_B be measured from the initial configuration of the mechanism upon assembly. θ_A and θ_B must be altered by the rotation of the input link, θ_i, in order to maintain the axial force parallel and the shear force perpendicular to the undeformed cable. The subsequent angles after a rotation of θ_i will be ϕ_A and ϕ_B as shown in Figure 4.2.

$$\phi_A = \theta_A - \theta_i$$
$$\phi_B = \theta_B + \theta_i$$

For static equilibrium, the force and moment balance on the output link yields.

$$\Sigma F_3 = 0$$

$$H_A\cos\phi_A + P_A\sin\phi_A + H_B\cos\phi_B - P_B\sin\phi_B = 0 \qquad (4.1)$$

$$P_A\cos\phi_A - H_A\sin\phi_A + P_B\cos\phi_B + H_B\sin\phi_B - mg = 0 \qquad (4.2)$$

$$\Sigma M_A = 0$$

$$-M_A - M_B + P_B L\cos(\phi_B-\theta_o) + H_B L\sin(\phi_B-\theta_o)$$

$$- mg\left(\frac{L}{2} - \delta\right)\cos\theta_o + \varepsilon\sin\theta_o = 0 \qquad (4.3)$$

Referring to Figure 4.3, the deflections of the cables are along a line perpendicular to the undeformed initial position, so that point A can be calculated from

$$A_x = -\ell_A\sin\phi_A - w_A\cos\phi_A$$

$$A_y = -\ell_A \cos\phi_A + w_A \sin\phi_A$$

Similarly,

$$B_x = \delta\cos\theta_i + \ell_B \sin\phi_B - w_B \cos\phi_B$$

$$B_y = \delta\sin\theta_i - \ell_B \cos\phi_B - w_B \sin\phi_B$$

The length of the bottom plate remains unchanged, thereby connecting the deflections w_A and w_B.

$$(B_x - A_x)^2 + (B_y - A_y)^2 = \ell_o^2 \qquad (4.4)$$

$$\frac{B_y - A_y}{B_x - A_x} = \tan\theta_o \qquad (4.5)$$

4.2.2 Derivation of beam equations

The cables have been assumed to be beams which are loaded primarily in tension. The important equations will be derived for one cable with the second cable being loaded in a similar way.

Referring to Figure 4.4, and taking moments about point p:

$$M_\ell - M + P(w_\ell - w) - H_\ell(\ell - u) = 0$$

$$-\frac{dM}{du} - P\frac{dw}{du} + H\frac{du}{du} = 0$$

or

$$\frac{dM}{du} + P\frac{dw}{du} = H$$

$$\frac{d^2M}{du^2} + P\frac{d^2w}{du^2} = 0$$

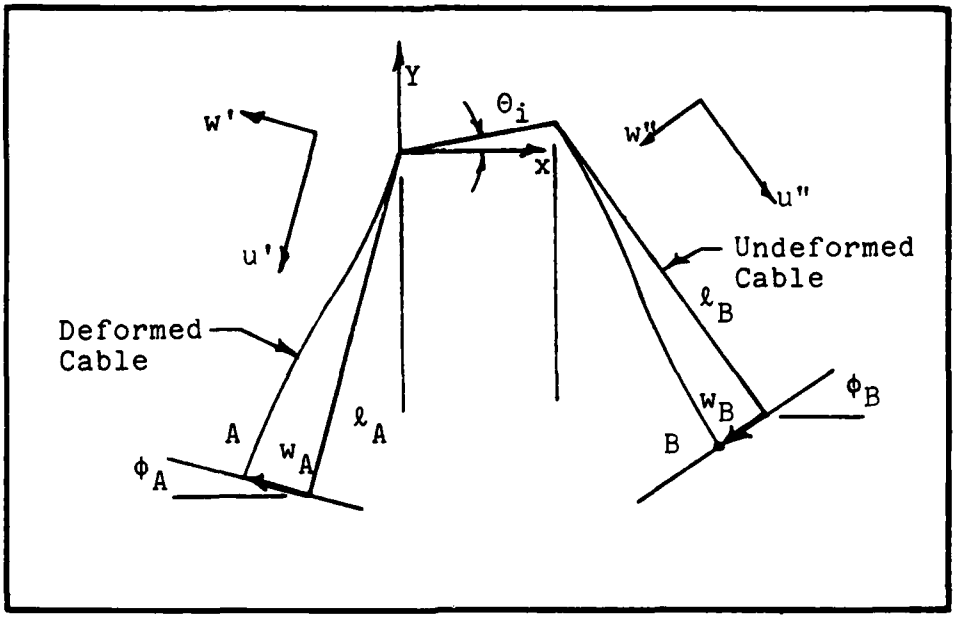

Figure 4.3 Deflection diagram for both cables as used for the position solution of points A and B.

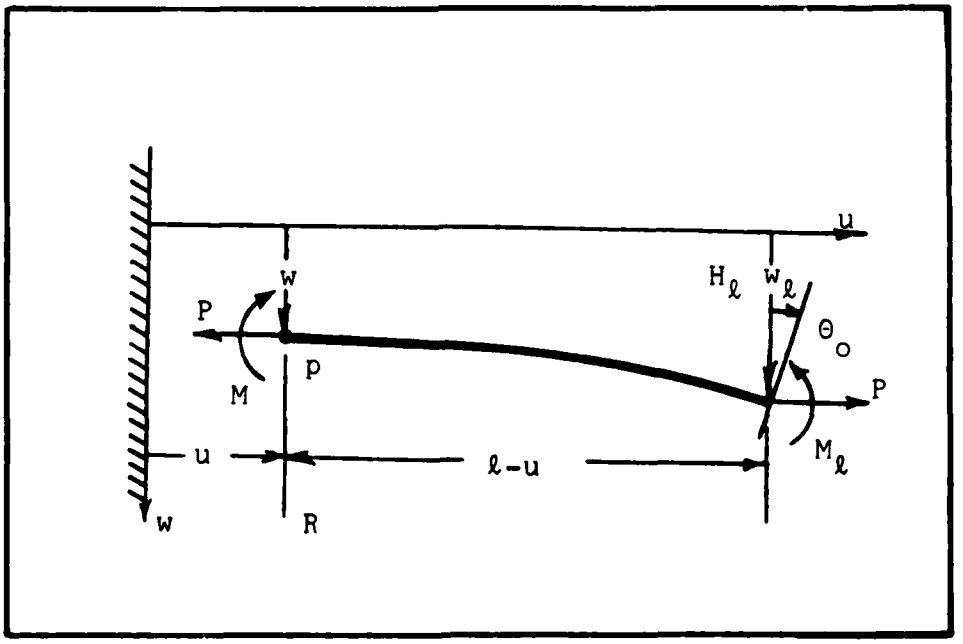

Figure 4.4 Free body diagrams for one cable indicating the variables in the beam equations.

Since the cables have been assumed to be Euler Bernoulli beams with small curvature, we can then write:

$$\frac{d^2w}{du^2} = -\frac{M}{EI}$$

$$\frac{d^2M_u}{du^2} - \beta^2 M_u = 0 \qquad \text{where} \qquad \beta^2 = \frac{P}{EI} \tag{4.6}$$

where EI is the flexural rigidity of the cable. The general solution of Equation 4.6 is

$$M_u = C_1 \cosh\beta u + C_2 \sinh\beta u$$

or

$$\frac{d^2w}{du^2} = -\frac{\beta^2}{P}(C_1 \cosh\beta u + C_2 \sinh\beta u) \tag{4.7}$$

As previously discussed in section 3.2.1, the boundary conditions will make use of the fact that the cables are nearly pinned at the input link and nearly clamped at the output link. The boundary conditions can be visualized with the aid of Figure 4.5 where the cable and plates are magnified to show the connections. The cable is firmly clamped at the bottom plate via a screw and washer. The cable at the top is drawn around a knife edge yielding a joint which has the aspect of being sensitive to plate rotation while not exerting a moment on the plate. So a pin joint is a reasonable approximation to the actual boundary conditions

The cables are not securely fastened to the input link at the knife edge. Since the attachment is away from the knife edge, a pinned condition occurs.

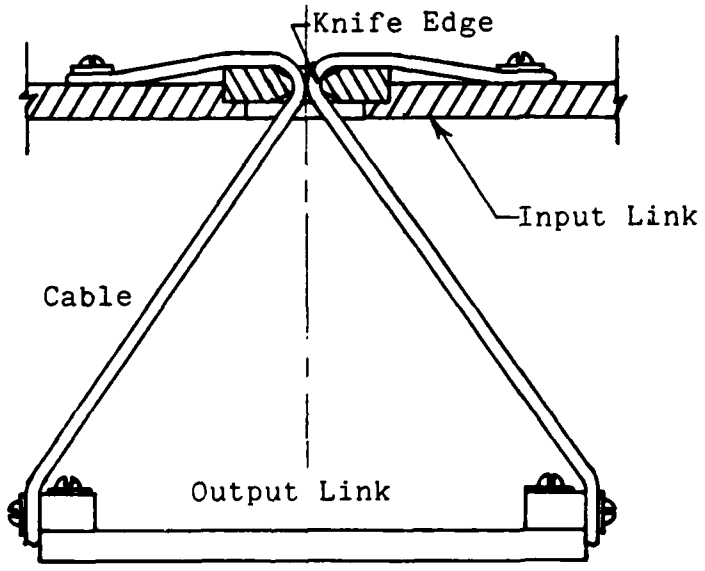

The cables are securely clamped to the output link by screws.

Figure 4.5 Sketch of the instrument illustrating the cable boundary conditions.

at the top link. The boundary conditions can then be stated as:

$$u = 0 \qquad w = 0 \qquad \frac{d^2w}{du^2} = 0$$

$$u = \ell \qquad \frac{dw}{du} = \theta_o \qquad \frac{d^2w}{du^2} = -\frac{M_\ell}{EI}$$

The above boundary conditions lead to the evaluation of the constants in Equation 4.7.

$$C_1 = C_4 = 0$$

$$C_2 = \frac{M_\ell}{\sinh\beta\ell}$$

$$C_3 = \theta_o + \frac{\beta M \cosh\beta\ell}{P \sinh\beta\ell}$$

Then the displacement and shear at the bottom of the cable can be found from equation 4.7 and its derivatives.

$$w_\ell = -\frac{1}{P}(C_1\cosh\beta\ell + C_2\sinh\beta\ell) + C_3\ell + C_4$$

Inserting the constants yields

$$w_\ell = \ell\theta_o + \frac{M_\ell}{P}\left[\frac{\beta\ell\cosh\beta\ell}{\sinh\beta\ell} - 1\right] \qquad (4.8)$$

From the equation for the shear on the cable

$$\frac{H}{EI} = \frac{d^3w}{du^3}$$

$$\frac{H_{\ell}}{EI} = \frac{H_{\ell}\beta^2}{P} = -\frac{\beta^3}{P}(C_1 \sinh\beta\ell + C_2 \cosh\beta\ell)$$

or

$$-\frac{H_{\ell}}{\beta} = C_1 \sinh\beta\ell + C_2 \cosh\beta\ell$$

Inserting the constants,

$$H_{\ell} = -M_{\ell}\beta\frac{\cosh\beta\ell}{\sinh\beta\ell} \qquad (4.9)$$

Equations 4.8 and 4.9 are then written for each cable. With the inclusion of equations 4.1 - 4.5 there are enough constraint equations to solve for the equilibrium position of the output link numerically.

4.3 Results from stiffness analysis

In order to evaluate the magnitude of the stiffness effects on K, the moment of inertia (I) and the modulus of elasticity (E) were found for a 0.006 in. diameter 7 X 1 stainless steel cable. The moment of inertia for the cable was calculated to be 4.494×10^{-11} in^4, while the modulus of elasticity was determined to be approximately 14×10^6 psi [3][4]. Stainless steel has a modulus of $28\text{-}29 \times 10^6$ psi, but a correction has been made for slippage and the reduced area of the cable as opposed to a solid wire. These values are only approximate as no experimental results were

[3] Costello, G.A.,etal,"Effective Modulus of Twisted Wire Cables", Journal of the Engineering Mechanics Division, ASCE, Vol. 102, No. EM1, February, 1976, pp. 171-181.

[4] Shigley, J.E.,"Mechanical Engineering Design", Third Edition, McGraw-Hill, New York, 1977.

obtained to confirm the moment of inertia or modulus of elasticity of the cable.

Figure 4.6 illustrates the influence of the stiffness on $\frac{1}{K}$ as a function of $\frac{\delta}{L}$ and $\frac{h}{L}$. The effect of $\frac{h}{L}$ is shown by successive plots starting with $\frac{h}{L} = 1/2$ (Figure 4.6a) and increasing up to $\frac{h}{L} = 10$, (Figure 4.6d). As with the earlier analysis, $\frac{h}{L} > 1$ has little effect on the input output ratio K. In fact, there is no difference between Figures 4.6c & d.

The $\frac{\delta}{L}$ ratio is plotted on each figure for what kinematically would be a pure pendulum, $\frac{\delta}{L} = 0$. K does not go to zero as it would in the kinematic analyses, but instead is a strong function of EI. It is apparent from Figure 4.6 that the kinematic influences at small $\frac{\delta}{L}$ ratios are negligible compared to the stiffness influences. As $\frac{\delta}{L}$ increases the kinematic errors begin to out weigh the stiffness errors. Therefore the earlier analyses are valid for small values of EI or for large values of $\frac{\delta}{L}$.

In Figure 4.7 the effects of $\frac{\varepsilon}{L}$ are illustrated. Figures 4.7a through 4.7d are based on $\frac{h}{L} = 1$ while $\frac{\delta}{L}$ is incremented on each plot. Again $\frac{\varepsilon}{L}$ has a strong influence on K and and to minimize the positioning error of the mechanism a large $\frac{\varepsilon}{L}$ is recommended.

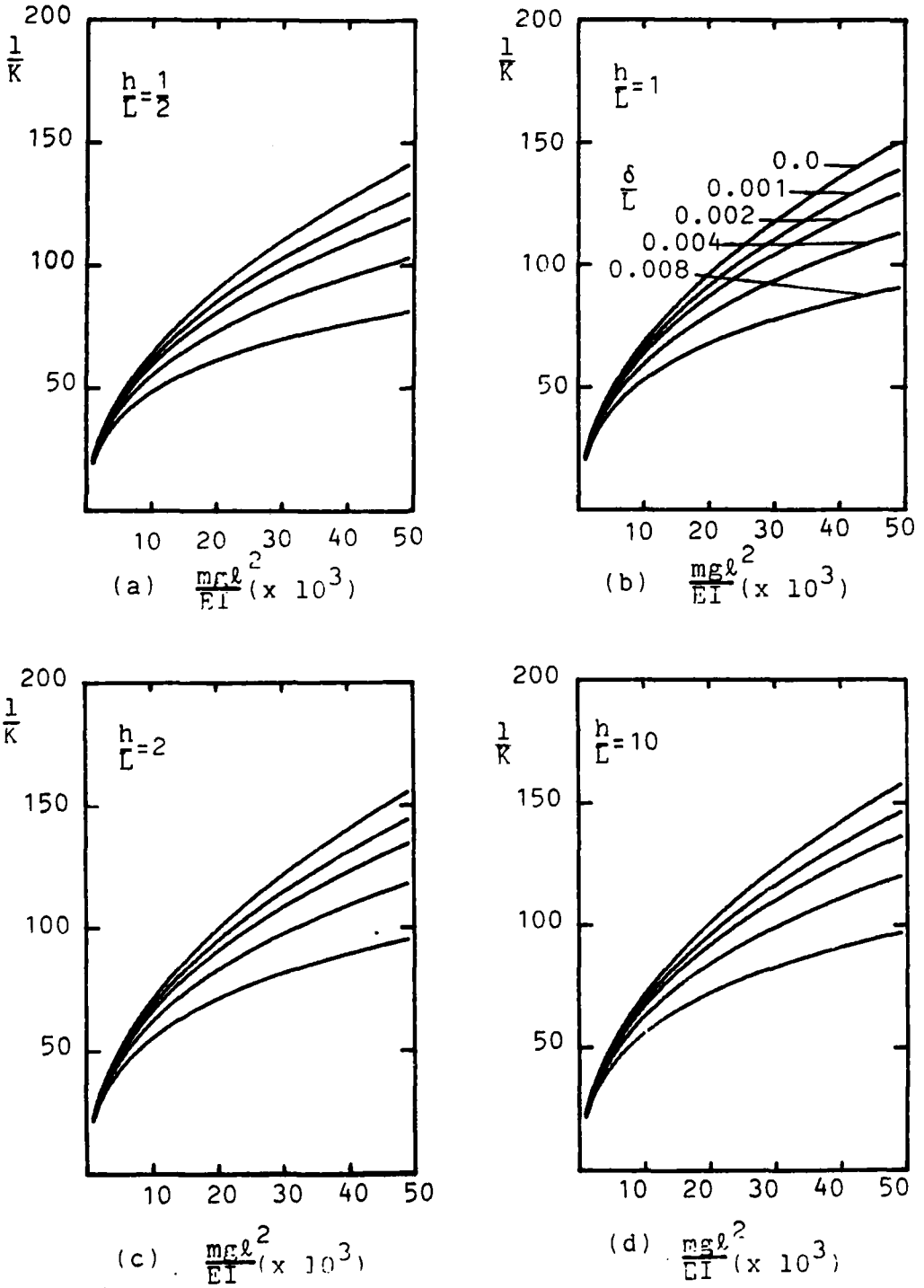

Figure 4.6 1/K vs $mg\ell^2/EI$ as a function of δ/L for varying h/L from planar analysis including stiffness.

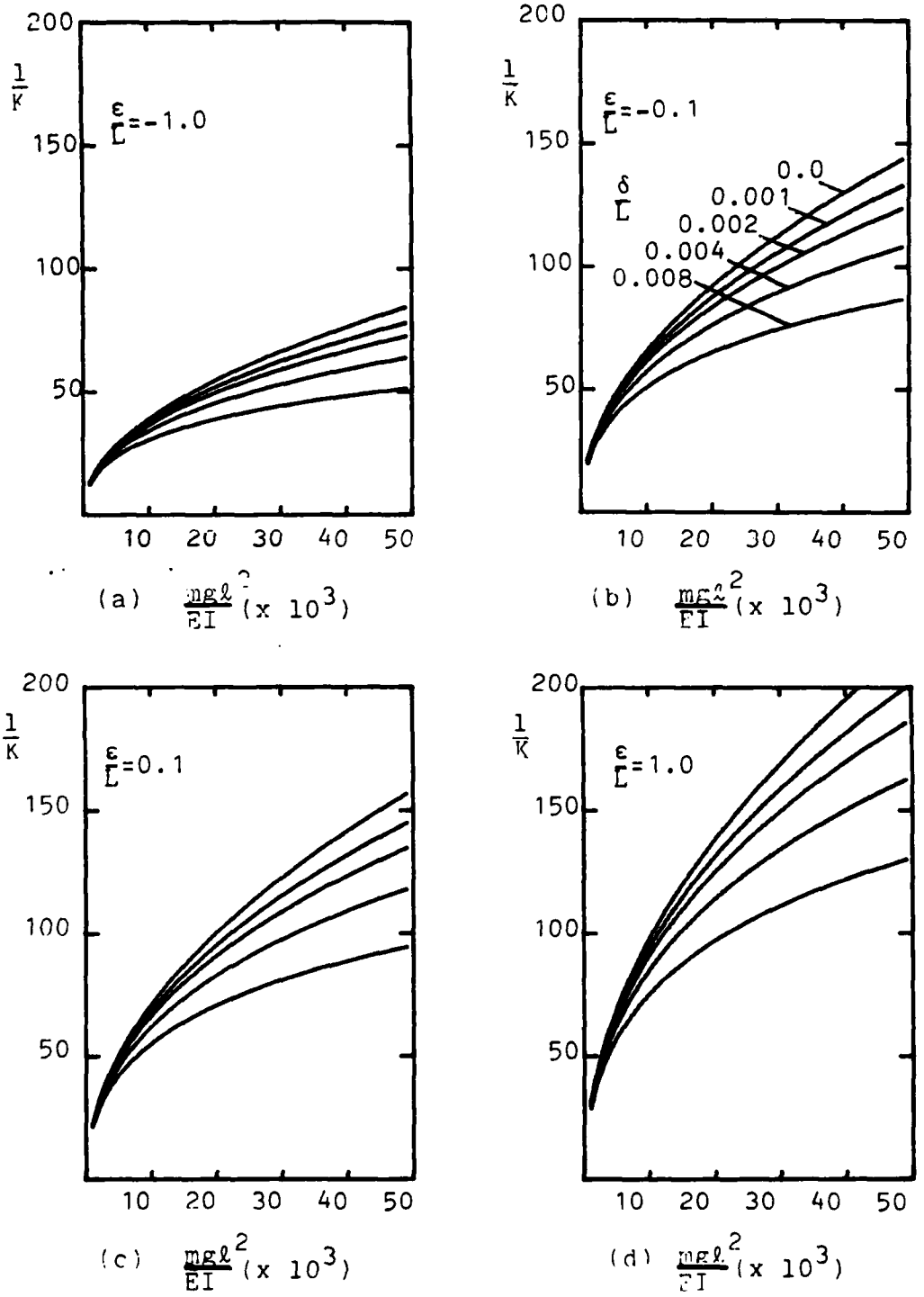

Figure 4.7 1/K vs $mg\ell^2/EI$ as a function of δ/L for varying ε/L from the planar analysis including stiffness.

In Chapter 2 it was shown kinematically that the CG could be located anywhere up to 50% of L along the output link without an associated error. The inclusion of stiffness into the kinematic model shows that Δ may vary widely without introducing any errors and also that the maximum limits are dependent on the cable stiffness.

Figures 4.8a,b illustrates $\frac{\Delta}{L}$ of 30% and 20% respectively. The curves do not differ from that of $\frac{\Delta}{L} = 0$, indicating that miscentering of the CG is not as critical as indicated in Chapter 2. Because the bending of the cables is creating a reactive moment on the output link the sign of Δ is important. If Δ is increased in the direction of the deflection, (i.e. to the left in Figure 4.4) the maximum value for $\frac{\Delta}{L}$ is approximately 30%. On the other hand, if Δ is negative with respect to the displacements, the maximum is close to 40% before the cables are loaded in compression. These results are dependent on EI and are stated for $\frac{mgl^2}{EI} = 1000$, or the first point plotted in Figure 4.8. As EI increases these values would increase to 50%.

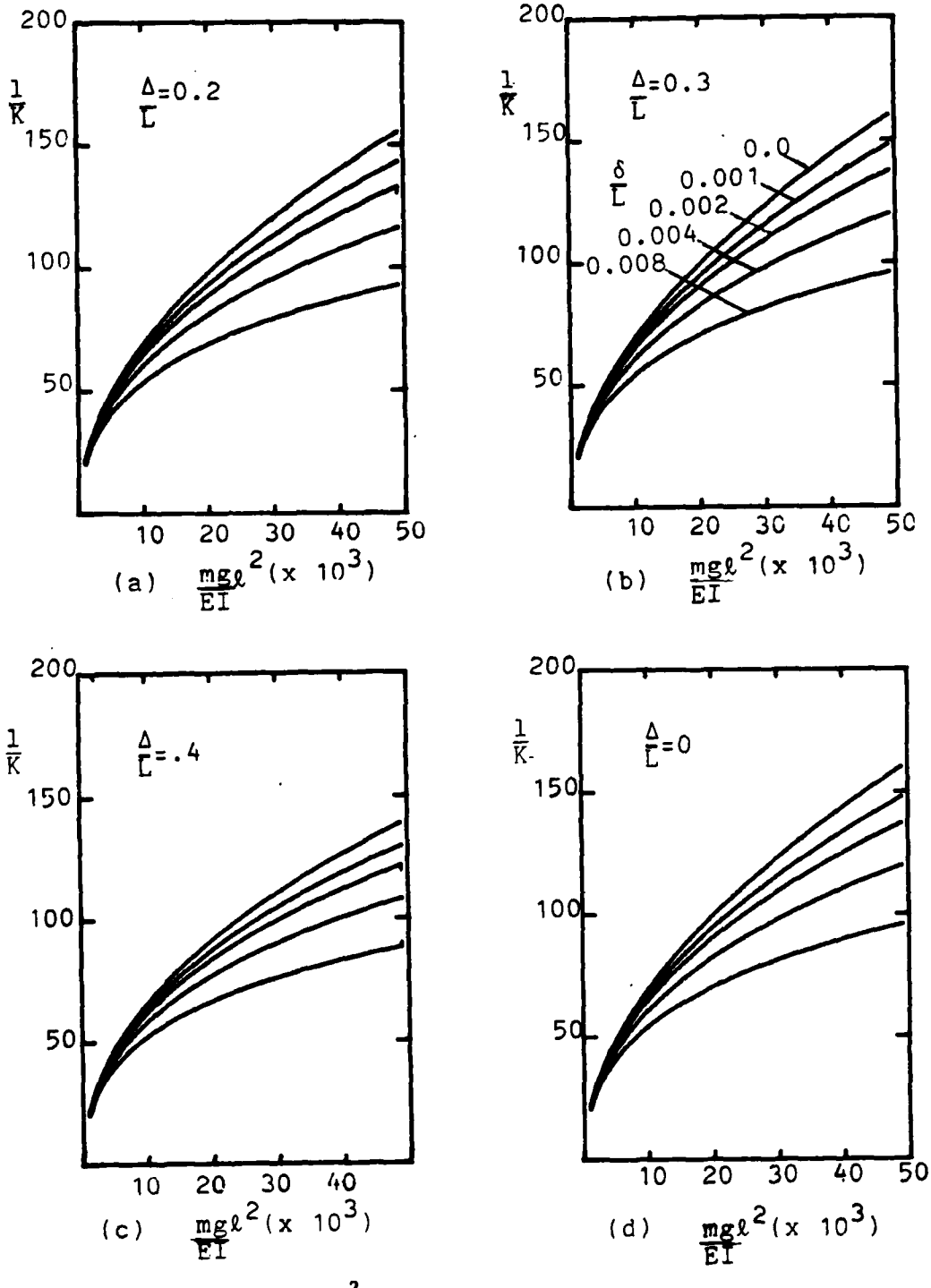

Figure 4.8 1/K vs $mg\ell^2/EI$ as a function of δ/L for varying Δ/L from the planar analysis including stiffness.

CHAPTER 5

EXPERIMENT

5.1 Objectives

Experimental results were needed to identify problems with the mechanism and to give a bench mark for the analytics. Three mechanisms were tested, two with a large input range and one for much smaller inputs. It was desired that these tests indicate the roles of the geometry of the mechanism, hence three different geometries.

5.2 Description of Experiments

The experimental procedure was divided into a small input test (for input motions from 10 to 300 arc-seconds) and a large input test (for rotations over 300 arc-seconds).

The small input test is shown in Figure 5.1a. An autocollimator was used to monitor both input (θ_i) and output (θ_o) by use of a beam splitter. The autocollimator enabled a 0.5 arc-second accuracy to be held on both the input rotations and the output rotations.

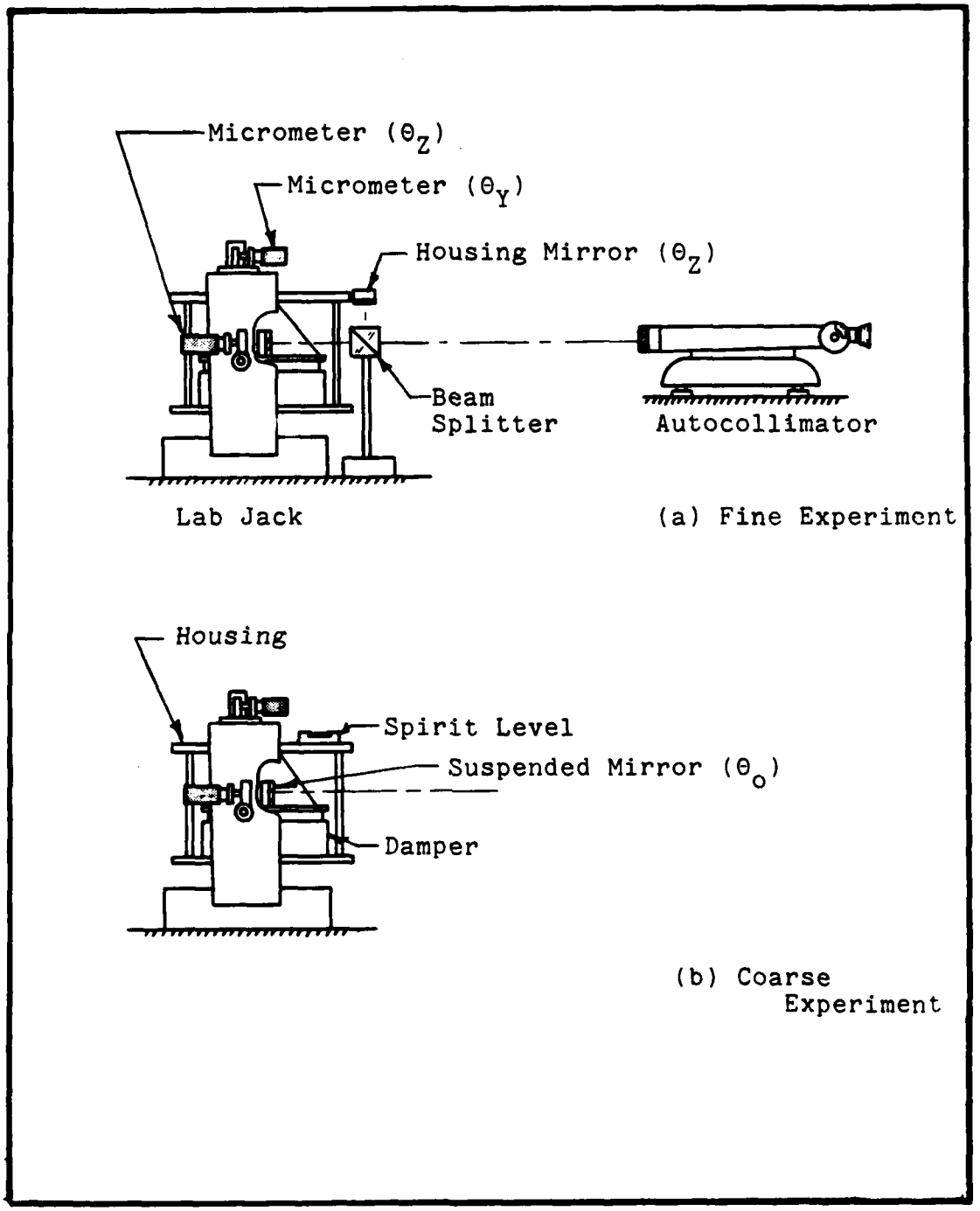

Figure 5.1 Sketch of apparatus used to determine K experimentally.

Since the autocollimator had only a ± 5 arc-minute range, the input rotations during the coarse experiment were monitored by using a spirit level with 5 arc-minute graduations as shown in Figure 5.1b Experimental procedures consisted of rotating the lab stand to a predetermined θ_Z via a micrometer and then reading the output angles by use of the autocollimator.

5.3 Results from Static Positioning Experiments

Tests were conducted on three mechanisms which are described by the table (Table 5.1) of non-dimensionless link lengths. The major differences between the mechanisms were the parameters (δ/L). Both of the cases A and B have relatively small input links (δ) compared to case C. The height (h) of A and B was again much smaller than C as indicated by the h/L ratio in the second column. Plus, the stiffness parameter $\frac{mgl^2}{EI}$ for case A was much smaller than cases B and C due primarily to an increased mass of these mechanisms.

Table 5.1
Non-Dimensional Ratios
Describing Experimental Mechanisms

Case	$\frac{\delta}{L}$	$\frac{h}{L}$	$\frac{\Delta}{L}$	$\frac{\varepsilon}{L}$	$\frac{mgl^2}{EI}$
A	0.0034	0.722	0.0	0.144	9342
B	0.0021	0.650	0.0	0.072	12160
C	0.0197	1.559	0.0	0.144	12160

5.3.1 Small input test

Eight experimental states are plotted in Figure 5.2 for the Case A mechanism along with the theoretical values from the planar kinematic and planar stiffness models. At each input state, an error band indicates the range of the measurements while the circle indicates the average. Linear regression yields the best fit line through the data and the slope of that line is K_{exp}. Comparisons of K_{exp} to the kinematic model of Chapter 1, K_{kin} and the kinematic model including cable stiffnesses, K_{stif} are then shown in Table 5.2.

It is apparent from Table 5.2 that the kinematic analysis yields a K which is extremely low in comparison to the experimental, with a difference of 78.6% from K_{kin} to K_{exp}. The second analysis gives a much better indicator of the performance of the mechanism with only a 13.4% difference between K_{exp} and K_{stif}. The primary reason for the large change between K_{kin} and K_{stif} is due to the small value of $\frac{\delta}{L}$. As seen in Chapter 4 Figure 4.6, the effects of the stiffness become predominant as $\frac{\delta}{L}$ becomes small.

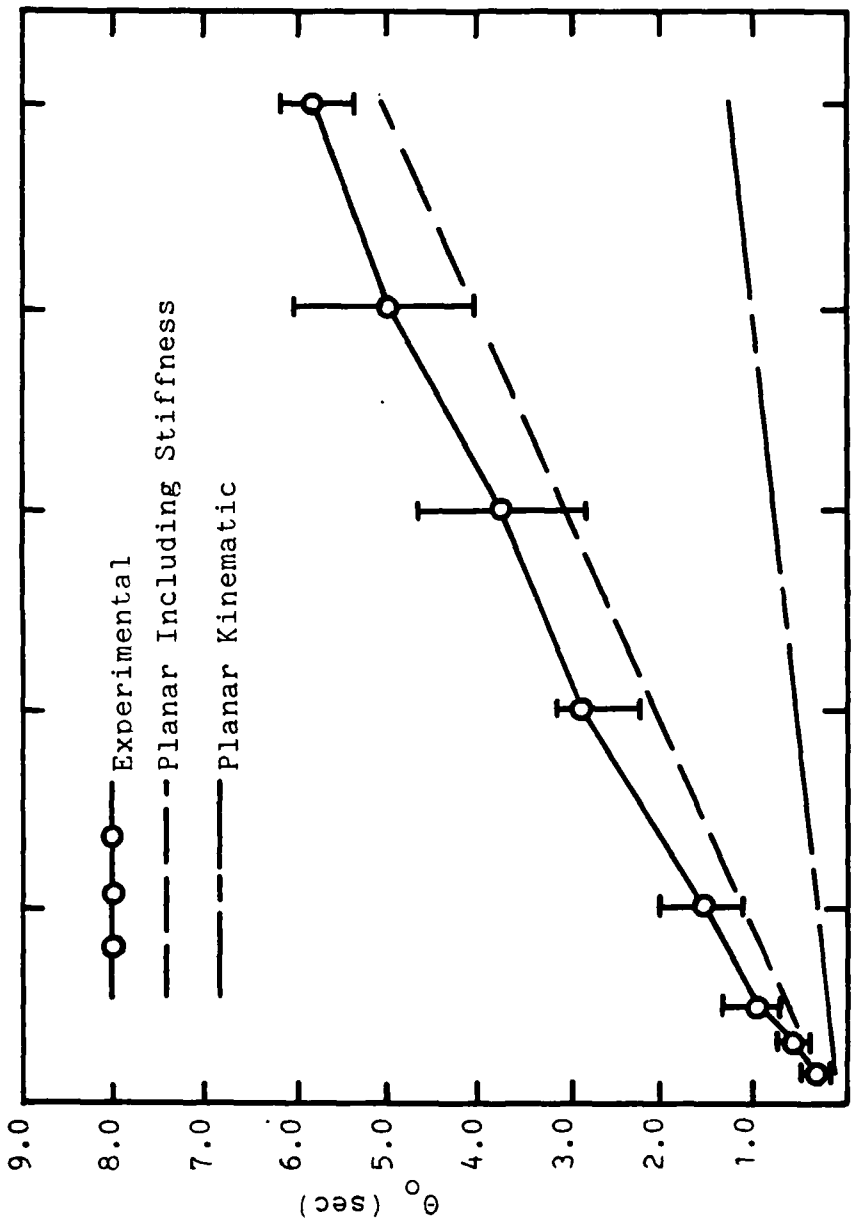

Figure 5.2 Results from the small input test for case A mechanism.

Table 5.2
Comparison of Results
for Experimental Mechanisms

Case	K_{exp}	K_{kin}	% Diff	K_{stif}	% Diff
A	0.0187	0.0040	78.6%	0.0162	13.4%
B	0.0124	0.0020	85.0%	0.0144	-16.1%
C	0.0194	0.0185	5.6%	0.0221	-13.9%

(% Diff. defined as $\frac{K_{exp} - K_{analysis}}{K_{exp}} \times 100\%$)

5.3.2 Large input test

The results from the large input test for case B are illustrated by the lower set of curves in Figure 5.3. Case B consistently has a smaller angular error (θ_0) than does Case C as predicted by the planar kinematic analysis of each. The kinematic analysis again predicts a lower K than that found experimentally, as indicated in Table 5.2 with a 85.6% difference of K_{kin} to K_{exp}. Although the stiffness model reflects the experimental data better, with a 16.1% difference from K_{stiff} to K_{exp}, it also predicts a larger value for K than that measured. This is surprising in view of the case A results where K_{kin} was larger than K_{exp}.

Turning to case C, illustrated by the upper set of curves in Figure 5.3, it is apparent that the planar kinematic analysis for this mechanism accurately predicts the experimental results with a difference of only 5.6% as

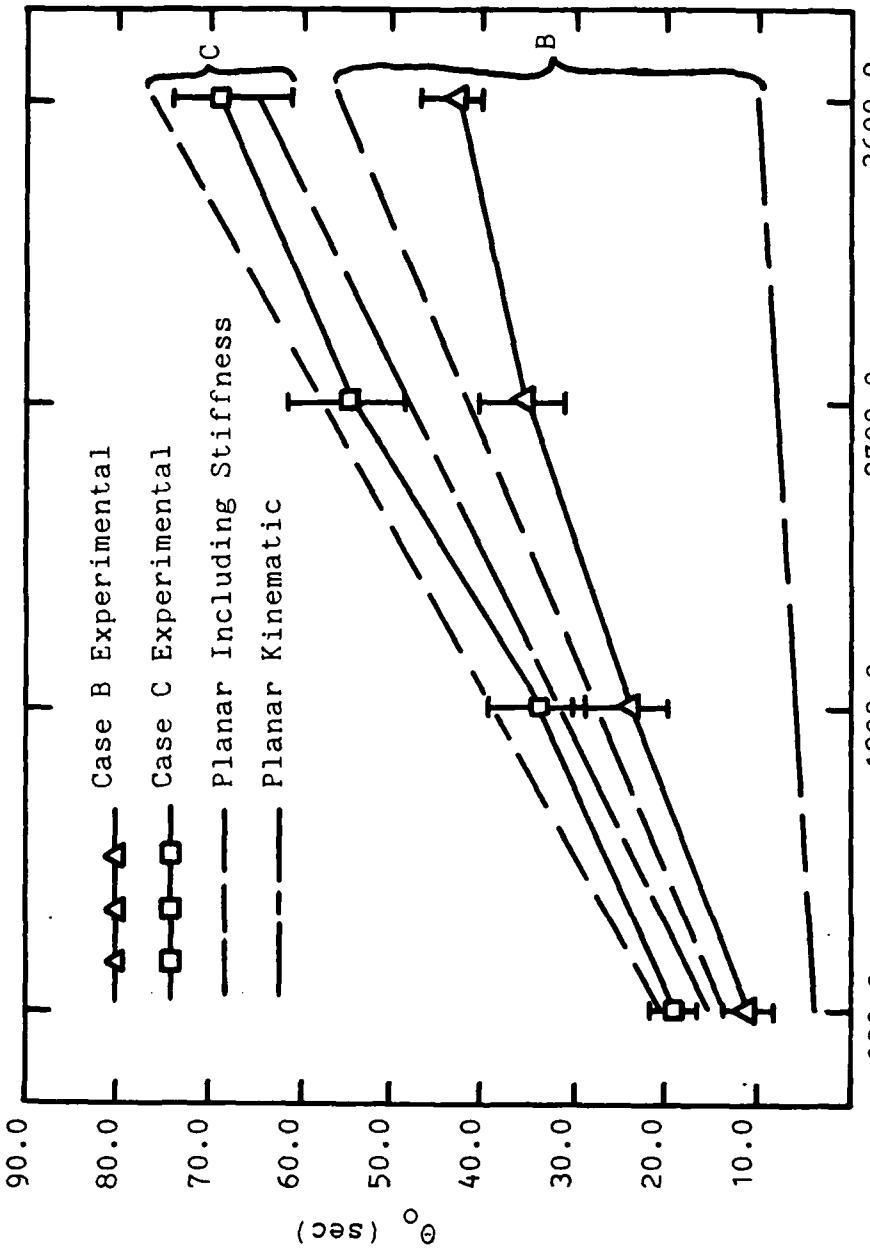

Figure 5.3 Results from the large input test for case B and C mechanisms.

shown in Table 5.2. This shows that the kinematic errors due to the large $\frac{\delta}{L}$ are outweighing the errors due to stiffness. The inclusion of stiffness in the analysis increases K_{stiff} to 0.0221, for a difference of 13.9% between K_{kin} and K_{stif} with the stiffness model again yielding the larger K.

5.3.3 Discussion of results and error sources

As mentioned previously, the symbols on the experimental curves reflect the average of the data at that point, while the error bands extend above and below these. The error band was as much as ± 30%, 15%, and 10% of the average values for cases A, B and C respectively. For case A the large spread is partially due to the resolution of the autocollimator (± .5 arc seconds) while a 1 arc second measurement was being made. Hence, an accuracy problem exists. For cases B and C the spirit level used to monitor the input could be read to ± 1 arc minutes, while the magnitude of the input angles were on the order of 1 degree. So it can be concluded that cases B and C were run with reasonable accuracy, while the data for case A could be different from the nominal values plotted in Figure 5.2 or listed in Table 5.2.

Since the stiffness analysis predicts K values greater than the experimental for cases B and C, it indicates that the analytics are incorrect or that some variable or values were incorrect. As mentioned in Section 3.3, the value of EI was merely an estimate. If EI were decreased by a small

amount K would decrease sizably since $\frac{mg\ell^2}{EI} = 14 \times 10^3$ is seen to lie on the rapidly increasing portion of the curve shown in Figure 3.6b. From this figure one sees that a decrease of E from 14 to 12 X 10^6, a decrease of 14%, would change K approximately 6%. Also, the difference between the planar and spatial analyses from Chapter 3 was roughly 10%, thereby reconciling the differences between the experimental results and the results from the kinematic model including stiffness as being dependent on the value for E and the rotations out of the plane of the planar analysis.

It should be noted that errors could be introduced in the planar analysis including stiffness where small deflections were assumed. Inherent in this assumption is that the distance along the undeformed cable, (u) from Chapter 4 Figure 4.7, remains constant and the deflections (w) are from the undeformed cable. The actual length of the cable is $\ell = \sqrt{u^2 + w^2}$. While this is a small effect, it would change K by 1% for example in Case C. So a more accurate analysis would be to assume large deflections of the cables.

The boundary conditions assumed for the cables, however, are the most representative of the actual situation. If a clamped condition were to be assumed at the input link, the system would be stiffer and raise K, while a pinned connection at the bottom would lower K, yet be unrealistic due to the firm attachments. Therefore, in comparison with the

experimental results it is shown that the boundary conditions are correct.

From the comparison of the experimental and analytical results it can be concluded that the analytics are refined sufficiently to be used as a design tool. And, as discussed in Chapter 7, a mechanism can be designed which has a positioning error of less than one arc second.

CHAPTER 6

DAMPER

6.1 Objectives

As previously mentioned, the level will be used in an environment in which vibrations are present due to the machine tool the instrument is monitoring and others in the surrounding production area. These vibrations must be eliminated by a damper because the leveling mechanism is passive and has no means of compensation. The characteristics looked for in the damper were: 1) the ability to function equally well in two orthogonal directions, 2) remove oscillations above 1% of the input (100 arc seconds nominally) and 3) not interfere with the function of the level.

These constraints lead to the cylindrical damper shown in Chapter 1 Figure 1.4, and again in Figure 6.1. Air will be used as the viscous medium not because it is the optimum, but because seals are not required and hence no friction will be introduced into the system to degrade the mechanisms positioning accuracy. The analytics developed herein will be used to determine the feasibility and then the design of

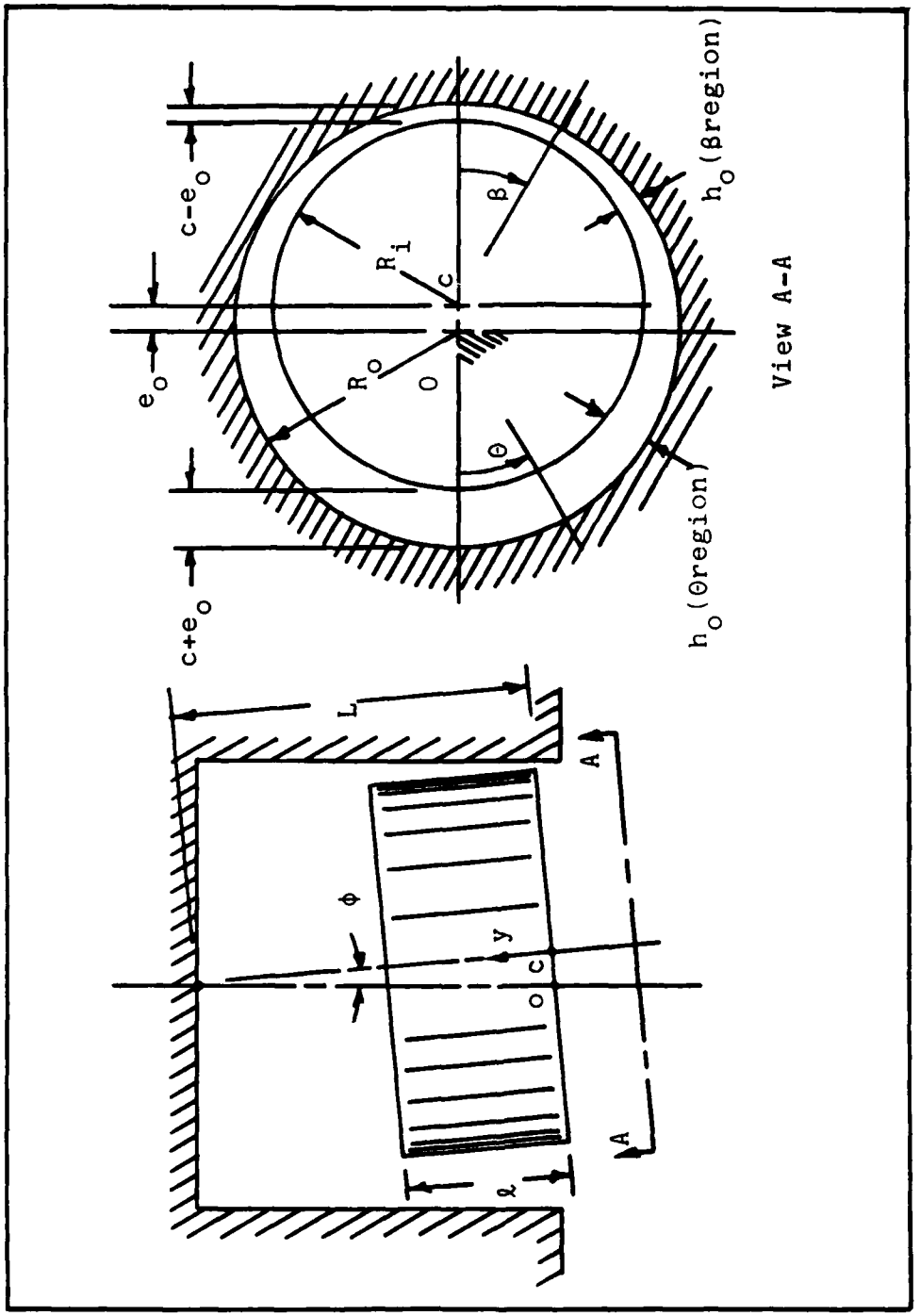

Figure 6.1 Illustration of the variables used to describe the cylindrical damper.

a cylindrical air damper for this application.

6.2 Cylindrical Pendulum Damper Mechanics

Equation 6.1 [5], the Reynolds Equation, defines the mechanics of a fluid between walls inclined to each other and moving relative to each other. It is assumed that the space between the walls is small enough to suggest that the flow is laminar and fluid velocity perpendicular to the walls is negligible compared to that parallel to the walls. These conditions prevail approximately if the ratio between the developed flow path length and the gap is better than 1000:1. The required ratio is even larger if the fluid viscosity is very low as is the case with air. As a beginning, approximations based on laminar flow conditions will be assumed even though the length-gap ratio may not be quite optimum.

Reynolds Equation:

$$\frac{\partial\left(\frac{h^3 \partial p}{6\mu \partial x}\right)}{\partial x} + \frac{\partial\left(\frac{h^3 \partial p}{6\mu \partial y}\right)}{\partial y} = f(x,y)$$

$$f(x,y) = -U\frac{\partial h}{\partial x} - W\frac{\partial h}{\partial y} + 2V \qquad (6.1)$$

See list of symbols for Chapter 6.

The Reynolds Equation can be written in polar coordinates consistent with the damper geometry. Further assuming constant viscosity of the air

[5] Cameron, A.,"Principles of Lubrication", J. Wiley Publ.

$$\frac{\partial(h^3\frac{\partial p}{\partial\theta})}{\partial\theta} + \frac{R^2\partial(h^3\frac{\partial p}{\partial y})}{\partial y} = 6\mu R^2\left| -U\frac{\partial h}{\partial y} - \frac{W\partial h}{R\partial\theta} + 2V\right| \qquad (6.2)$$

at any level y the gap h can be written as

$$h = c + e(y)\cos\theta \quad \text{or} \quad h = c - e(y)\cos\beta$$

To get a general estimate of the mechanism behavior, it is advisable to non-dimensionalize important parameters. For the pendulum damper, the following transformations are convenient.

$$H(y) = \frac{h(y)}{h_o} \qquad \varepsilon(y) = \frac{e(y)}{c}$$

$$a = \frac{h\ (y=\ell) - h\ (y=0)}{h\ (y=0)} = \left[\frac{H_\ell - H_o}{H_o}\right]\beta \text{ region}$$

$$b = \frac{h\ (y=0) - h\ (y=\ell)}{h\ (y=\ell)} = \left[\frac{H_o - H_\ell}{H_\ell}\right]\theta \text{ region}$$

$$Y = \frac{y}{\ell}$$

In a pendulum damper, the U and W velocities are ineffectual compared to the squeeze component V so that Equation 6.2 can be simplified and with the non-dimensional transformation becomes

$$\frac{\partial(H^3\frac{\partial p}{\partial\theta})}{\partial\theta} + (\frac{R}{\ell})^2\frac{\partial(H^3\frac{\partial p}{\partial y})}{\partial Y} = \frac{6\mu R^2}{h_o^3}[-0\ -0\ +2V]$$

The above partial differential equation can not be solved in a closed form but a simplification suggests itself

by the realities of tilting dampers. Because h varies along y it is not practical to use long damper cylinders. If, on the other hand, short cylinders are used ($\frac{\ell}{2R} < \frac{1}{2}$) it might be assumed that pressure gradients in the circumferential direction will be considerably less than in the axial direction. If that is the case, the first expression on the left hand side of the Reynolds Equation might be ignored reducing the partial differential equation to the ordinary differential equation 6.3.

$$\frac{d(H^3\frac{dp}{dY})}{dY} = \frac{12\mu v\ell^2}{h_o^3} \qquad (6.3)$$

where the squeeze velocity around the cylinder is described as

$$V = \dot{\phi}(L-y)\cos\Theta = \dot{\phi}L(1-Y\frac{\ell}{L})\cos\Theta$$

and

$$V = \dot{\phi}L(1-Y\frac{\ell}{L})\cos\beta$$

therefore

$$\frac{\partial(H^3\frac{dp}{dY})}{dY} = \frac{12\mu\dot{\phi}L}{C^3}(1-Y\frac{\ell}{L})\cos\beta$$

Let

$$P = (\frac{h_o}{12\mu\dot{\phi}L\ell^2})p = D\ p$$

so that

$$\frac{d(H^3\frac{dP}{dY})}{dY} = (1-Y\frac{\ell}{L})\cos\beta$$

Since $Y\frac{\ell}{L} < 1$ let us expedite the search for behavior characteristics by setting the right hand side to $(1 - 0)\cos\beta$. A refined analysis with $Y\frac{\ell}{L}$ included might be pursued later.

Reduced Reynolds Equation:

$$\frac{d(H^3\frac{dP}{dY})}{dY} = \cos\beta \qquad (6.4)$$

At any position β integrating 6.3 yields

$$\frac{\frac{dP}{dY}}{\cos\beta} = \frac{Y}{H^3} + \frac{C_1}{H^3}$$

Integrating again

$$\frac{1}{\cos\beta}P = \int \frac{Y}{H^3}dY + C_1\int \frac{dY}{H^3} + C_o \qquad (6.5)$$

From the non-dimensional transformations in the β region

$$H = 1 + aY$$

therefore

$$Y = \frac{H-1}{a} \qquad \& \qquad dY = \frac{dH}{a}$$

Substituting the above into Equation 6.4 yields

$$\frac{P}{\cos\beta} = \frac{1}{a^2}\int \frac{(H - 1)dH}{H^3} + \frac{C_1}{a}\int \frac{dH}{H^3} + C_o$$

$$\frac{a^2P}{\cos\beta} = [-\frac{1}{H} + \frac{1}{2H^2}(1 - \frac{C_1a}{2}) + C_oa^2]$$

or

$$\frac{a^2 P}{\cos\beta} = -\frac{1}{H} + \frac{\lambda_1}{H^2} + \lambda_o$$

at

$$y = \ell, \quad Y = 1, \quad H = H_\ell, \quad P = 0$$

$$y = 0, \quad Y = 0, \quad H = H_o, \quad P = 0$$

Then

$$\lambda_1 = \frac{H_\ell H_o}{2H_c} \qquad \& \qquad H_c = \frac{H_o + H_\ell}{2}$$

$$\lambda_o = \frac{1}{2H_c}$$

Therefore

$$\frac{a^2}{\cos\beta} P = -\frac{1}{H} + (1 + \frac{H_\ell H_o}{H^2})\lambda_o \qquad (6.6)$$

At any position β a strip $Rd\beta$ wide, of the damper cylinder, has a force dF exerted on it:

$$dF = \int_0^\ell pRd\beta dy = \frac{Rd\beta\ell}{D} \int_0^\ell PdY$$

$$dF = \frac{R\ell\cos\beta d\beta}{a^3 D} \int_{H_o}^{H_e} -\frac{1}{H} + (1 + \frac{H_e H_o}{H^2})\lambda_o \, dH$$

$$dF = \frac{R\ell\cos\beta d\beta}{a^3 D}\left[-\ln(1+a) + \frac{a}{2+a}\right]$$

The force component in the direction of the eccentricity change is

$$dZ = dF\cos\beta = \frac{R\ell\cos^2\beta d\beta}{a^3 D}\left[-\ln(1+a) + \frac{a}{2+a}\right]$$

In the region $-\pi < \beta < \frac{\pi}{2}$ the total force generated is

$$Z = \frac{2R\ell}{D} \int_0^{\frac{\pi}{2}} \frac{\cos^2\beta}{a^3}\left[-\ln(1 + a) + \frac{a}{2 + a}\right] d\beta$$

$$a = \frac{H_\ell(\beta) - H_o(\beta)}{H_o(\beta)} = \frac{\Delta H(\beta)}{H_o(\beta)}$$

where

$$\Delta H(\beta) = \ell\phi\cos\beta \qquad \& \qquad H_o(\beta) = 1 - \varepsilon_o\cos\beta$$

and

$$\frac{1}{D} = \frac{12\mu\dot{\phi}L\ell^2}{h_o^3}$$

Therefore

$$Z = 24\mu\dot{\phi}LR\ell^3 \int \frac{\cos^2\beta}{a^3 h_o^3}\left[-\ln(1+a)+\frac{a}{2+a}\right] d\beta$$

$$Z = \frac{24\mu\dot{\phi}LR\ell^3}{(\ell\phi)^3} \int_0^{\frac{\pi}{2}} \frac{1}{\cos\beta}\left[-\ln(1+a) + \frac{a}{2+a}\right] d\beta$$

$$\ell\phi = c\varepsilon = \frac{cL\varepsilon}{L} \qquad \& \qquad \dot{\phi}L = V_o$$

or

$$Z = 24\mu V_o R\left(\frac{\ell}{c}\right)^3\left(\frac{L}{\ell\varepsilon_o}\right)^3 \int_0^{\frac{\pi}{2}} \frac{1}{\cos\beta}\left[-\ln(1 + a) + \frac{a}{2 + a}\right] d\beta$$

A similar treatment to the θ region yields an analogous result with suction, rather than positive pressure, being generated, hence, the two regions reinforce each other so that the total fluid force becomes

$$F = 24\mu V_o R(\frac{\ell}{c})^3 K_D$$

where

$$K_D = (\frac{L}{\ell\varepsilon_o})^3 \int_0^{\frac{\pi}{2}} \frac{1}{\cos\theta}\left[-(\ln(1+a) + \ln(1+b)) + \frac{a}{2+a} + \frac{b}{2+b}\right] d\theta$$

$$a = \frac{\ell\varepsilon_o\cos\theta}{L(1-\varepsilon_o\cos\theta)}$$

$$b = \frac{\ell\varepsilon_o\cos\theta}{L(1+\varepsilon_\ell'\cos\theta)} \qquad \varepsilon_\ell' = \varepsilon_o(1-\frac{\ell}{L})$$

K_D is given on Figure 6.2 as a function of the eccentricity ratio ε_o and length ratios $\frac{\ell}{L}$. At $\varepsilon_o = 0$ the pendulum is exactly centered on it's cylindrical housing. At $\varepsilon = 1.0$ the pendulum is touching the wall. The minimum damping force occurs at $\varepsilon = 0$

There were several approximations made to expedite the analysis. While the results are not exact, the errors are probably sufficient for design purposes and they do show the role of the important parameters.

6.3 Pendulum with Fluid Damping

As a convenient but reasonable approximation to the actual 3 dimensional dynamics, a 2 dimensional analysis was developed. A sketch of the damper system is shown in Figure 6.3.

Taking moments about the pivot 0 (a fixed instantaneous center of curvature rather than the perturbated small movement was assumed):

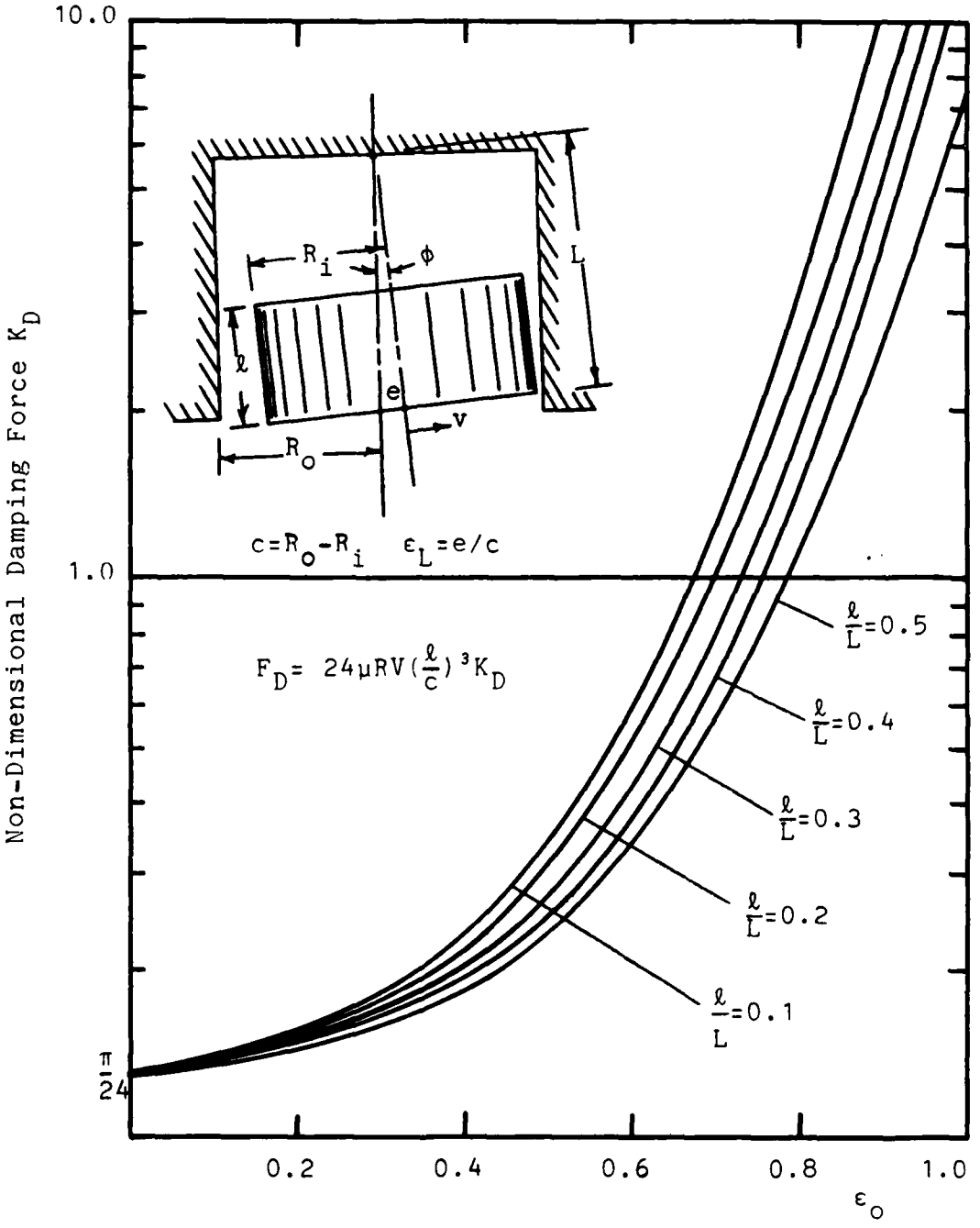

Figure 6.2 Damping force vs. the eccentricity ratio ε_o as a function of the length ratios ℓ/L.

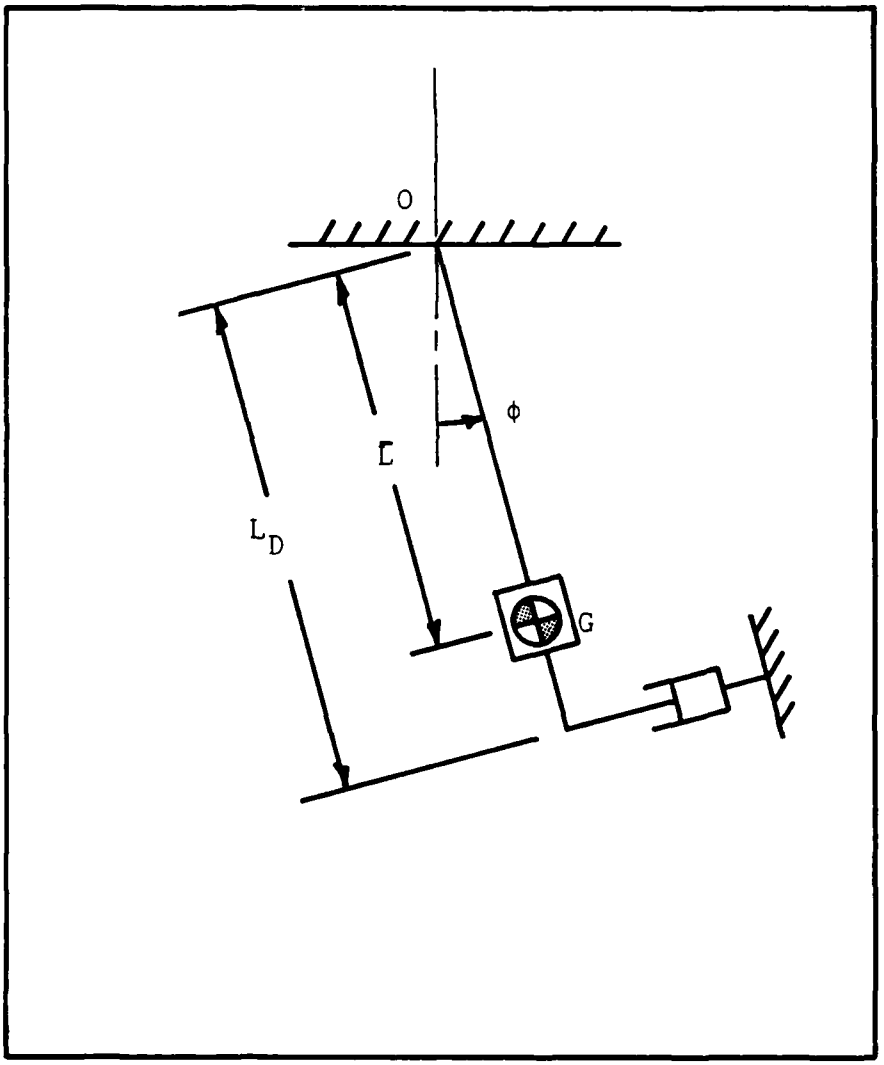

Figure 6.3 Schematic representation of the damper motions about a fixed pin joint O.

$$\Sigma M_o = mg\bar{L}\sin\phi - C_D L_D \dot{\phi} = J\ddot{\phi}$$

Hence

$$J\ddot{\phi} + C_D L_D^2 \dot{\phi} + mg\bar{L}\sin\phi = 0$$

or for small motion,

$$\ddot{\phi} + \frac{C_D}{J} L_D^2 \dot{\phi} + \frac{mg}{J} \bar{L}\phi = 0 \qquad (6.7)$$

The undamped natural frequency of the pendulum ω_n is:

$$\omega_n^2 = mg\frac{\bar{L}}{J} = \frac{g}{\bar{L}(1+(k/\bar{L})^2)} \qquad (6.8)$$

The damping factor:

$$\zeta = \frac{C_D L_D^2}{2J\omega_n} = \frac{C_D \omega_n L_D}{\frac{L_D}{\bar{L}}}$$

$$\zeta = \frac{C_D L_D^2}{2m(\bar{L})^{1.5}\sqrt{g(1+(k/\bar{L})^2)}} \qquad (6.9)$$

The damping force is described as $F_D = C_D V$ but from Section 6.1 F_D is also described as

$$F_D = 24\mu RV(\frac{\ell}{c})^3 K_D \qquad (6.10)$$

Hence

$$C_D = 24\mu R(\frac{1}{c})^3 K_D \qquad (6.11)$$

Substitution of this into Equation 6.9 yields

$$\zeta = 24\mu R(1/c)^3 \times \frac{\omega_n L_D^2}{2mg\bar{L}} \times K_D \qquad (6.12)$$

6.4 Experiment

Equation 6.12 demonstrates the design parameters and their role for acquiring a working damping coefficient. This was used to construct the experimental apparatus of Figure 6.4. The experiment was fairly simple in that the only instrumentation required was a laser. The laser was directed to a mirror attached on the mechanism and then on to a sheet of graph paper positioned at the correct height. By virtue of the distance from the mirror to the graph paper, a magnification of the mirror rotations occur, such that up the laser beam was displaced about 6 cm. for a one degree swing of the mirror. Then the cusps of the laser beam were marked on the paper as the time was recorded.

The experimental damper was sized as shown in Figure 6.5. The damping ratio was then determined as follows. The clearance (c) is

$$c = \frac{D_o - D_i}{2} = .0135$$

Substituting the data in Figure 6.3 into Equation 6.12 yields

$$\zeta = 24 \times 0.25 \times 10^{-8} \times 1.875\left(\frac{.5}{.0135}\right)^3 \times \frac{11.4}{2 \times 0.72} \times \frac{2.56^2}{2.66} \times K_D$$

or

$$\zeta = 0.11\ K_D$$

At $\varepsilon = 0$, $K_D = \frac{\pi}{24}$ (Figure6.2); $\zeta = .014$

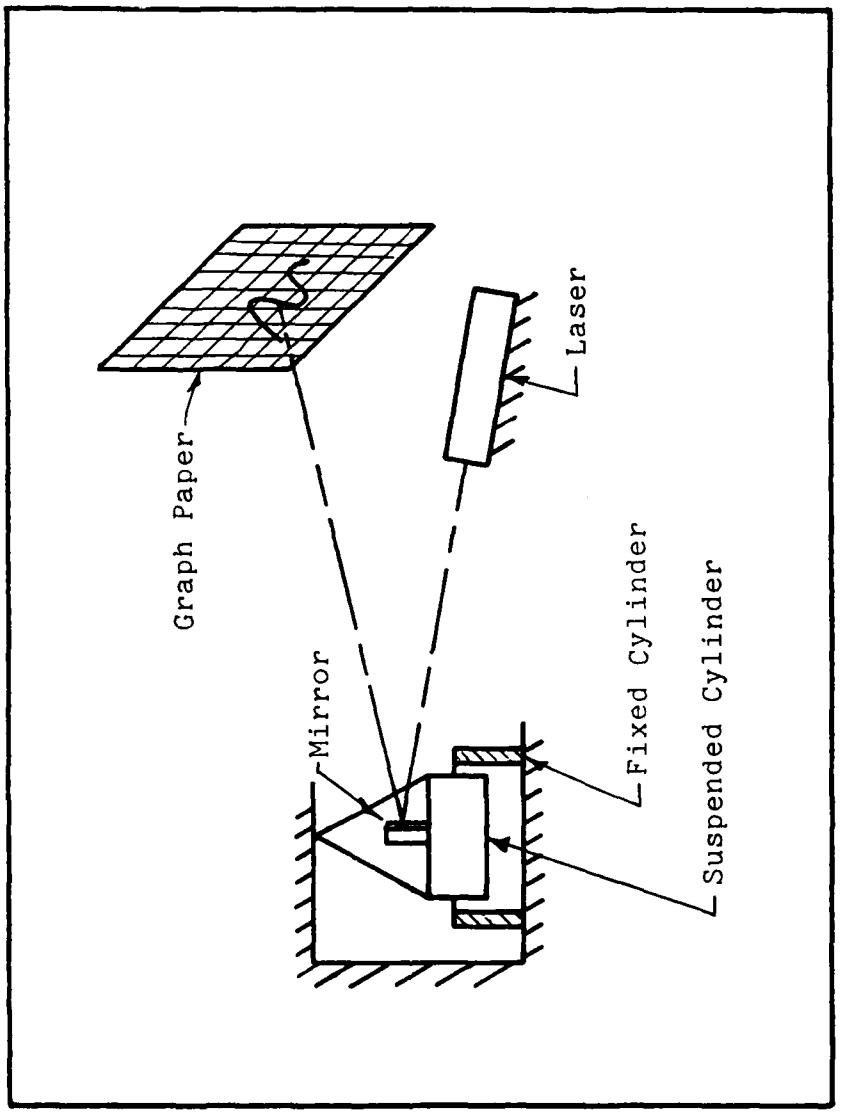

Figure 6.4 Sketch of apparatus for determining ζ experimentally.

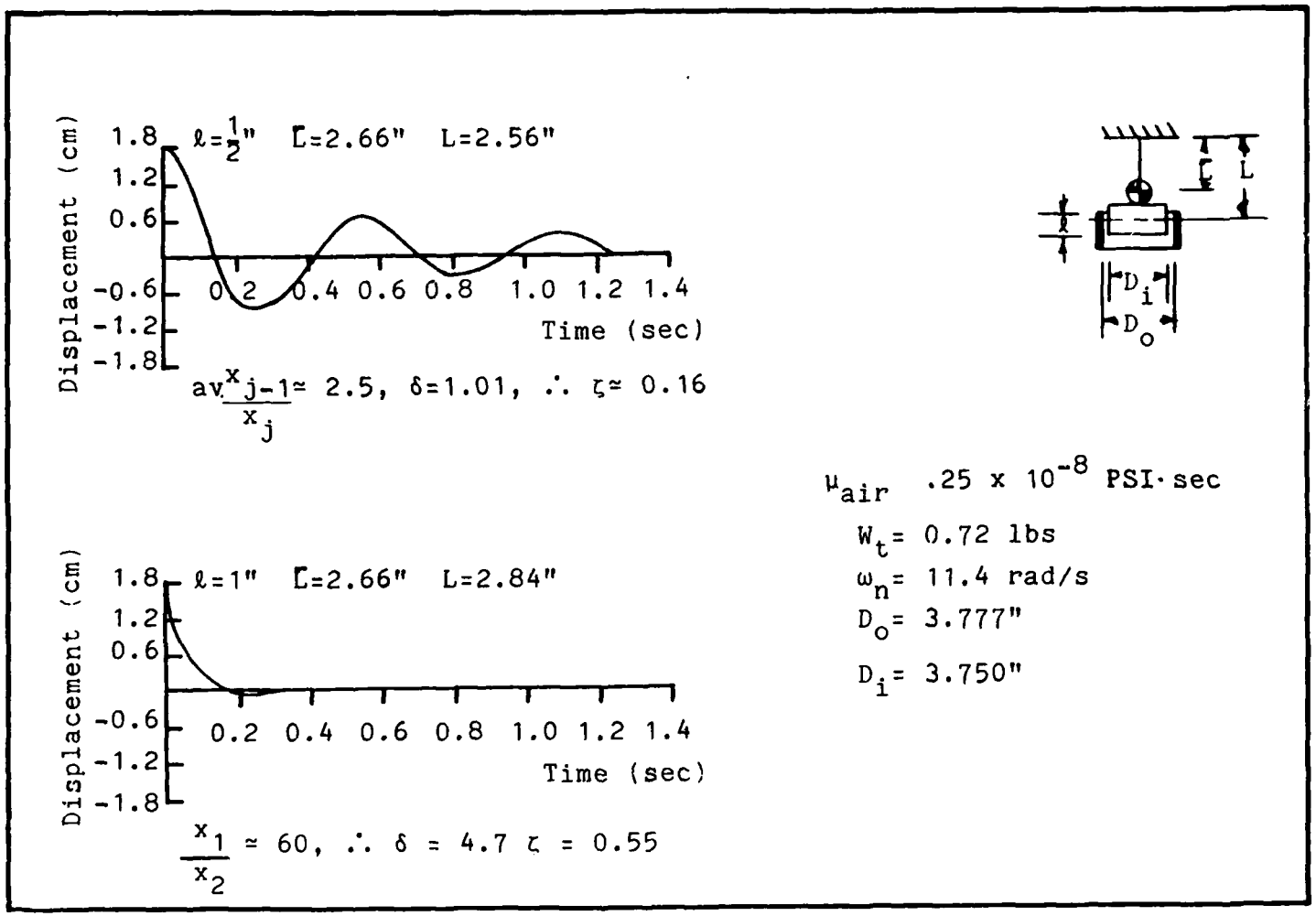

Figure 6.5 Results from experimental pendulum damper for two cases.

and at $\varepsilon = 0.7$; $\ell = \frac{.5}{2.56} = .2$; $K_D = 0.85$

If ℓ is increased to 1" and every other property is unchanged then

$$\zeta = \left(\frac{1}{.5}\right)^3 \times \left(\frac{2.84}{2.50}\right)^2 \times .11K_D$$

and

at $\varepsilon = 0$ $\zeta = .14$ at $\varepsilon = 0.7$ $\zeta = .93$

6.5 Experimental Results

The first experiment was conducted with $\ell = 0.5$". The response, Figure 6.4a, indicates $\zeta = 0.17$. A second experiment with $\ell = 1.0$ yielded the response of Figure 6.4b and $\zeta = 0.73$. The experimental set up did not allow a determination of the eccentricity in the dormant state, furthermore, the resolution possible was coarser than $\varepsilon = 0.3$.

Experimental ζ and theoretical ζ are 0.17 and 0.094 respectively, from the first test ($\ell = 0.5$"). Experimental and theoretical ζ are 0.55 and 0.93, respectively from the second test ($\ell = 1.0$"). Theoretical values were based on a 0.3 eccentricity between damper sleeves considering that the test set up static ε is only an estimate and the fact that the rapid decay of oscillations makes it difficult to measure the second and third decayed amplitudes; agreement with theory seems adequate for design purposes.

Equations 6.12 with Figure 6.2 should serve as adequate design guides. From Equation 6.11 it is apparent that to maximize damping the following parameters should be considered.

1. The wetted length to radial clearance ratio $\frac{\ell}{c}$ is very critical coming in as a cubic influence.

2. The ratio $\frac{L_D^2}{\bar{L}^{1.5}}$ calls for setting L_D as long as possible and $\bar{L}$ as short as possible. By the kinematics of the suspension it is suggested that maximizing $\bar{L}$ may serve both.

3. Both the mass and to a lesser degree the radius of gyration should also be minimized.

Finally, one might ask how small a value of ζ is tolerable. In other words, how long will it take the pendulum to subside to a motion 1% of the initial disturbance. This decay rate is approximated by

$$n = \frac{1}{\zeta} \ln 100 = \frac{\ln 100}{2\pi\zeta} = \frac{.73}{\zeta}$$

n = number of oscillations.

If the period of the pendulum is .6 secs and ζ = .1 the time interval is 4.4 seconds. If a 1 second interval is desirable the required damping factor must be .44. Hence it

is possible to design an air damper which will have a settling time of 1 second. Also, the size of the damper required for this example is reasonable. The size of the damper is not prohibitive given the size of the output link, both nearly 3.75 inches.

CHAPTER 7

CONCLUSIONS

A proposed mechanism to level optics about two horizontal axes to a high degree of accuracy has been studied to determine the structural properties that influence the operation. The mechanism is composed of two ternary links, one being the input with the other, the output, being suspended by miniature cables. The mechanism was designed to simulate a spherical pendulum so that output rotations would be less than 1 arc second for input rotations up to 100 arc seconds.

Initially, the 3 dimensional mechanism was generalized to the two dimensional case. A kinematic analysis was performed the two dimensional model to highlight the effects of link lengths and tolerances on the positioning errors. From this analysis it was learned that the ratio of the output link length to the input link length was an important parameter. This ratio must be maximized, up to 1000:1, to get a desirable performance from the mechanism. The vertical position of the center of mass was also an important system parameter and should lie below the bottom link to ensure

minimum kinematic error. A surprising result from this analysis was that the center of mass need not be centered on the output link due to the assembly procedure of the mechanism.

Upon comparison of the results from this analysis with results gathered in experiments, it was found that the planar model predicted lower output angles for two of the three experimental mechanisms. It was hypothesized that the difference was due to rotations of the output link which were unaccounted for in the planar model.

A spatial kinematic analysis was then performed which included all of the geometry found in the experimental mechanism. While the analysis was far longer than the planar, a small amount of additional information was gathered. The important result was that the actual 3 dimensional mechanism has less positioning errors than indicated by the planar analysis due to rotations of the output link about the vertical axis having a corrective action on the rotations about the horizontal axes. The spatial analysis checked well enough with the planar to indicate the former could be done with little loss in accuracy. Since the spatial analysis indicates lower output angles than the previous analysis, there is a greater discrepancy with the experimental data.

The effects of stiffness in the mechanism due to the

bending effects of the support cables were then investigated to understand the difference observed between the analytical and experimental results. The support cables were thought to be slender beams pinned at the input link and clamped at the output link on the two dimensional representation of the mechanism. This analytical approach proved to accurately predict the output observed in the experimental work. It was found that the effects of the moment of inertia and modulus of elasticity of the cables were stronger parameters to the system, for certain geometries, than the kinematic properties. It was shown that these variables increased the output angle exponentially such that the minimum modulus and inertia must be used to optimize the performance of the mechanism.

An air damper was also designed to minimize disturbances of the optics during operation. Two cylinders, one fixed to the output link and one to ground, formed a two dimensional damper which was free of friction while dissipate the input oscillations effectively. Again, in order to establish the correct geometry, an analysis based on the Reynolds Equation assuming constant air viscosity was performed. Using experimental results from two damper geometries, it was shown that the analysis was adequate to characterize the system, and that the cylinder length should be maximized while the distance from the input link to the center of gravity of the optics should also be maximized.

RECOMMENDATIONS

To optimise the performance of a two-axes level the following should be considered.

1. The stiffness ratio $\frac{mg^2}{EI}$ should be maximized. The two possible ways to do this are reduce the cable diameter, reduce the moment of inertia, or increase the wire length. By reducing the cable diameter, δ may also be reduced and by increasing the wire length, the height (h) is increased both yielding better performance by reducing the stiffness effects and kinematic effects. The mass on the output link should not be raised because this would reduce the damping ratio.

2. Maximize the height (h) of the mechanism. As illustrated in Chapters 2 and 4, the h/L ratio is the next important variable after δ/L and the stiffness ratio. Certainly one would not elect to make h/L much less than unity, as K increases rapidly after this point. The damping ratio is inversly proportional to the height, Equation 6.12, while K runs expodentially with h, Figures 4.1,4.2 and 4.3, so one must comprimise the settling time for the positioning error, but the minimum h/L should still be in the area of unity.

3. Section 6.3 indicates that the center of mass should be above the center of the damping force, or the center of the wetted length of the cylinder, and the further away the better for maximized damping. From Chapters 2 and 4 one would like the center of mass below the connection point of the cables to the output link to minimize the positioning errors. Hence, the center of mass should lie between the cable connections on the output link and the center of the wetted length to satisfy both the settling time and the positioning errors.

4. The centering of the mass on the ouput link was shown to be unimportant to the functioning of the mechanism in Chapters 2 and 4. However, the miscentering does effect the assembly of the mechanism to the damper. The horizontal shift of the output link is equal to the miscentering, so that the assembly tolerance of the mechanism to the damper equals the tolerance on the location of the mass center.

APPENDICES

APPENDIX A

Planar Kinematic Program Listing

The following program was developed to determine the equilibrium position of a four bar mechanism with a mass attached to one link. The program calculates the wire lengths (r2 & r4) required to make the output link (r3) level initially. This requires the user to supply the lengths of the input (r1) and the output links, an initial rotation (wint), a misscentering of the optics on link 3 (u) and the height of the mechanism (h), all of which determine the lengths of the wires. The instant center 1/3 is then positioned directly above the center of mass on the output link. A non-linear equation solver is then called to solve the eight constraint equations describing the location of the pin joints, points A and B. The equation solver is a routine in the International Mathematics & Statisics Library and it calls an external subroutine fcn. The program was written in Fortran F77.

```
      program main(input,output,tape5=input,tape6=output)
c
c     Planar model using Newtonian static equilibrium.
c     Length of wires, links 2 and 4 are calculated
c     based on an initial rotation of link 1 and a
c     miscentering of the cg on link 3.
c     Up-dated on Jan 2 1984
```

```
c
      dimension par(1),wk(600),xo(8),xa(8)
      common/data/r1,r2,r3,r4,r5,r6,cx,cy,dx,dy
      real gx,gy
      external fcn,fun
      n=8
      m=150
c
      pi=acos(-1.0)
      deg=180./pi
c        Variables describing link lengths are read
      read(5,*) r3,r1,dist,ph,wint,u
      win=wint/deg
c        Translate link 1 until the IC is above the CG
      ax=-r3/2.+u
      ay=0
      bx=r3/2.+u
      by=0
      cpx=ax*r1*(ph*cos(win)+bx*sin(win))/(bx*(ph+r1*sin(win))-ph*ax)
      cpy=ph
      dpx=cpx+r1*cos(win)
      dpy=cpy+r1*sin(win)
      gx=0.0
      gy=ay-dist
c      Determine the lengths of links 2, 4, 5 & 6
      r2=sqrt((ax-cpx)**2.+(ay-cpy)**2.)
      r4=sqrt((bx-dpx)**2.+(by-dpy)**2.)
      r5=sqrt((gx-ax)**2.+(gy-ay)**2.)
      r6=sqrt((gx-bx)**2.+(gy-by)**2.)
c      Initial estimate of independent variables
      xo(1)=ax
      xo(2)=ay
      xo(3)=bx
      xo(4)=by
      xo(5)=gx
      xo(6)=gy
      xo(7)=1/2.
      xo(8)=1/2.
c          Output indicating initial configuration
      write(6,2)
      2    format(1h1)
      write(6,10) r1
      10   format(6x,13horiface dia =,f7.4)
      write(6,20) r2,r4
      20   format(6x,17hlength of wires =,f7.4)
      write(6,30) r3
      30   format(6x,8hstance =,t7.4)
      write(6,35) dist
      35   format(6x,13hplate to cg.=,f7.4)
      write(6,36) ph
      36   format(6x,8hneight =,f7.4)
      write(6,38) wint
      38   format(6x,21hinitial angular error,f7.4)
```

```
      write(6,39) u
      39  format(6x,9hcg. error,t7.4)
      write(6,40)
      40  format(///,8x,7htheta g,6x,7htheta m,6x,7htheta 2,
     ! 6x,7htheta 3,5x,9hd theta m)
c     read thé number of input states to be
c     solved, l.  Read the input state tint(deg)
      read(5,5) l
      5   format(i2)
      do 100 j=1,l
      read(5,*) tint
      tin=tint/deg
      cx=cpx+r1*cos(tin)/2.
      cy=cpy-r1*sin(tin)/2.
      dx=dpx-r1*cos(tin)/2.
      dy=dpy+r1*sin(tin)/2.
c     Non-linear equation solver
      call zscnt(fcn,10,n,m,par,xo,fnorm,wk,ier)
c     Calculate the rotation of link 3
c     from points ay and by.
      ay=xo(2)
      by=xo(4)
      tho=asin((by-ay)/r3)
      tout=tho*deg*3600.
c     Calculate the input output ratio rat
      if(tint.ne.0.0) then
       rat=tho*deg/tint
      else
       rat=0
      endif
c
      write(6,60) tint,tout,rat,xo(7),xo(8)
     60   format(/,3x,5f13.5)
     100  continue
c
      stop
      end
c
c     Subroutine containing constraint equations
c
      subroutine fcn (x,f,n,par)
      common/data/r1,r2,r3,r4,r5,r6,cx,cy,dx,dy
      dimension x(n),f(n),par(1)
      real gx,gy
      ax=x(1)
      ay=x(2)
      bx=x(3)
      by=x(4)
      gx=x(5)
      gy=x(6)
      fca=x(7)
      fdb=x(8)
c
```

```
      f(1)=(ax-bx)**2. + (ay-by)**2. - r3**2.
      f(2)=(ax-cx)**2. + (ay-cy)**2. - r2**2.
      f(3)=(bx-dx)**2. + (by-dy)**2. - r4**2.
      f(4)=(ax-gx)**2. + (ay-gy)**2. - r5**2.
      f(5)=(bx-gx)**2. + (by-gy)**2. - r6**2.
      f(6)=(cx-ax)*fca/r2 + (dx-bx)*fdb/r4
      f(7)=(cy-ay)*fca/r2 + (dy-by)*fdb/r4 -1.
      f(8)=((bx-ax)*(dy-by) - (by-ay)*(dx-bx))*fdb/r4
     ! -(gx-ax)
      return
      end
```

AD-A160 151 MECHANICS OF A TWO AXES PASSIVE PRECISION LEVEL MONITOR 2/2
FOR MACHINE TOOLS VOLUME 2(U) PURDUE UNIV LAFAYETTE IN
J D YORK ET AL. MAY 85 N00014-83-K-0385

UNCLASSIFIED F/G 14/2 NL

END
FILMED
DTIC

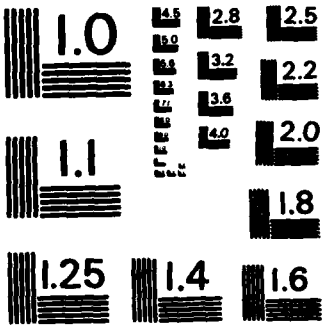

APPENDIX B

Spatial Kinematic Program

This program was developed to perform a spatial kinematic position solution for a five bar mechanism with spherical joints and a mass fixed to one link. The input to the program are the lengths of the input links (r1, r2, r3), the height of the mechanism (ph), the lengths of the output links (r4, r5, r6), the miscentering of the cg along the X axis (u) and the vertical distance from the output plate to the cg (dist). The program calculates the wire lengths based on the above variables and an initial rotation of the top plate.

A subroutine (rotate) calculates the final position of the top spherical joints via a rotation matrix. The output rotations are calculated based on Rodrigue's formula and the normal to points d, e, and f. As before, a non-linear equation solver is used to find the equilibrium of the mechanism and requires subroutine fcn.

```
program main(input,output,tape5=input,tape6=output)
real nx,ny,nz,h,hp,knx,kny,knz,kn
dimension xo(15),wk(1104),par(1),xp(15),n(3),hp(3)
```

```
! ,ztp(3),ytp(3),xtp(3),xt(3),yt(3),zt(3)
 common/data/r1,r2,r3,r4,r5,r6,r7,r8,r9,r10,r11,r12
! ,xt,yt,zt
 external fcn
c
c
c xd=x(1)  xe=x(4)  xf=x(7)  xcg=x(10)  fda=x(13)
c yd=x(2)  ye=x(5)  yf=x(8)  ycg=x(11)  feb=x(14)
c zd=x(3)  ze=x(6)  zf=x(9)  zcg=x(12)  ffc=x(15)
c
c
  n=15
  m=150
c
  pi=acos(-1.0)
  deg=180./pi
c
c     initial conditions, calculate the geometric center
c     of the top  plate and then points a, b, and c.
c
  read(5,*) r1,r2,r3
  read(5,*) r4,r5,r6
  read(5,*) dist,ph,u
  phi12=acos((r1**2.+r2**2.-r3**2.)/(2*r1*r2))
  phi13=acos((r1**2.+r3**2.-r2**2.)/(2*r1*r3))
  phi23=pi-phi12-phi13
  phi45=acos((r4**2.+r5**2.-r6**2.)/(2*r4*r5))
  phi46=acos((r4**2.+r6**2.-r5**2.)/(2*r4*r6))
  phi56=pi-phi45-phi46
c
  tp=pi/2-phi23
  rp=r1/(2*cos(tp))
  tb=pi/2-phi56
  rb=r4/(2*cos(tb))
c
  xtp(1)=-rp*cos(tp)
  ytp(1)=0.0
  ztp(1)=rp*sin(tp)
  xtp(2)=0.0
  ytp(2)=0.0
  ztp(2)=-rp
  xtp(3)=rp*cos(tp)
  ytp(3)=0.0
  ztp(3)=rp*sin(tp)
c      Initial estimate for points d, e, f and g, also forces
  xo(1)=-rb*cos(tb)
  xo(2)=ph
  xo(3)=rb*sin(tb)
  xo(4)=0.0
  xo(5)=ph
  xo(6)=-rb
  xo(7)=rb*cos(tb)
  xo(8)=ph
```

```
      xo(9)=rb*sin(tb)
      xo(10)=u
      xo(11)=ph+dist
      xo(12)=0.0
      xo(13)=0.33333
      xo(14)=0.33333
      xo(15)=0.33333
c          Normal to lower plate initially
      h(1)=xo(1)
      h(2)=xo(2)+1.
      h(3)=xo(3)
c          Store for initial position
      do 11,i=1,15
      11  xp(i)=xo(i)
c           Initial rotation of top plate
      read(5,*) wxint,wzint
      call rotate(xtp,ytp,ztp,xt,yt,zt,wxint,wzint)
      do 90 i=1,3
       xtp(i)=xt(i)
       ytp(i)=yt(i)
       ztp(i)=zt(i)
      90  continue
c          Calculate wire lengths and CG constraint links
      r7=sqrt((xo(1)-xtp(1))**2.+(xo(2)-ytp(1))**2.+(xo(3)-ztp(1))**2.)
      r8=sqrt((xo(4)-xtp(2))**2.+(xo(5)-ytp(2))**2.+(xo(6)-ztp(2))**2.)
      r9=sqrt((xo(7)-xtp(3))**2.+(xo(8)-ytp(3))**2.+(xo(9)-ztp(3))**2.)
      r10=sqrt((xo(10)-xo(1))**2.+(xo(11)-xo(2))**2.+(xo(12)-xo(3))
     ! **2.)
      r11=sqrt((xo(10)-xo(4))**2.+(xo(11)-xo(5))**2.+(xo(12)-xo(6))
     ! **2.)
      r12=sqrt((xo(10)-xo(7))**2.+(xo(11)-xo(8))**2.+(xo(12)-xo(9))
     ! **2.)
c             Input rotation of top plate, do (l) times
      write(6,170)
      write(6,175)
      read(5,10) l
      10  format(i2)
      do 350 j=1,l
      read(5,*) omegx,omegz
      call rotate(xtp,ytp,ztp,xt,yt,zt,omegx,omegz)
c             Call equation solver
      call zscnt (fcn,9,n,m,par,xo,tnorm,wk,ier)
c              Rodrigue's formula
      xha=(xo(8)-xo(2))*(xo(6)-xo(3))-(xo(5)-xo(2))*(xo(9)-xo(3))
      yha=(xo(4)-xo(1))*(xo(9)-xo(3))-(xo(7)-xo(1))*(xo(6)-xo(3))
      zha=(xo(7)-xo(1))*(xo(5)-xo(2))-(xo(4)-xo(1))*(xo(8)-xo(2))
      tl=sqrt(xha**2.+yha**2.+zha**2.)
      hp(1)=xo(1)+xha/tl
      hp(2)=xo(2)+yha/tl
      hp(3)=xo(3)+zha/tl
c
      knx=(xo(2)-xp(2))*(hp(3)-h(3))-(hp(2)-h(2))*(xo(3)-xp(3))
      kny=(hp(1)-h(1))*(xo(3)-xp(3))-(xo(1)-xp(1))*(hp(3)-h(3))
```

```
      knz=(xo(1)-xp(1))*(np(2)-n(2))-(np(1)-n(1))*(xo(2)-xp(2))
      kn=sqrt(knx**2.+kny**2.+knz**2.)
      nx=knx/kn
      ny=kny/kn
      nz=knz/kn
      s1=(n(1)-xp(1))*(np(1)-xo(1))+(n(2)-xp(2))*(np(2)-xo(2))+(n(3)-
     ! xp(3))*(np(3)-xo(3))
      s2=(n(1)-xp(1))*nx+(n(2)-xp(2))*ny+(n(3)-xp(3))*nz
      s3=(n(2)-xp(2))*nz-(n(3)-xp(3))*ny
      s4=(n(3)-xp(3))*nx-(n(1)-xp(1))*nz
      s5=(n(1)-xp(1))*ny-(n(2)-xp(2))*nx
      s6=s3**2.+s4**2.+s5**2.
      beta=acos((s1-(s2**2.))/s6)
      thetax=beta*nx*deg*3600.
      thetay=beta*ny*deg*3600.
      thetaz=beta*nz*deg*3600.
      thdm=sqrt(thetax**2.+thetaz**2.)
      thin=sqrt(omegx**2.+omegz**2.)
c     Calculate input output ratio rat
      if(thin.ne.0.0) then
       rat=thdm/(thin*3600.)
      else
       rat=0.0
c     Create new normal if the first one was superseded
      n(1)=xo(1)
      n(2)=xo(2)+1.
      n(3)=xo(3)
      do 305, i=1,15
     305   xp(i)=xo(i)
      endif
      write(6,174) thdm,omegx,omegz,rat,fnorm,thetay
     350  continue
c
c         output
c
      write(6,130) r1,r2,r3
      write(6,160) r4,r5,r6,ph
      write(6,190) r7,r8,r9
      write(6,135)
      write(6,140) (xtp(i),i=1,3)
      write(6,140) (ytp(i),i=1,3)
      write(6,140) (ztp(i),i=1,3)
      write(6,145)
      write(6,140) (xt(i),i=1,3)
      write(6,140) (yt(i),i=1,3)
      write(6,140) (zt(i),i=1,3)
      write(6,165)
      write(6,140) xo(1),xo(4),xo(7),xo(10)
      write(6,140) xo(2),xo(5),xo(8),xo(11)
      write(6,140) xo(3),xo(6),xo(9),xo(12)
      write(6,180) wxint,wzint
     130  format(1h15x,'upper plate dimensions:',/10x,'r1=',f10.4,
     ! 3x,'r2=',f10.4,3x,'r3=',f10.4)
```

```
 145   format(/,22x,'a',14x,'b',14x,'c')
 140   format(10x,4f15.5)
 135   format(/,21x,'ap',13x,'bp',13x,'cp')
 150   format(/,5x,'input rotation was: (deg.)',/10x,2f10.2)
 160   format(/,5x,'lower plate dimensions:',/10x,'r4='
 !  ,f7.3,3x,'r5=',f7.3,3x,'r6=',f7.3,3x,'h=',f7.3)
 165   format(/21x,'d',14x,'e',14x,'f',14x,'cg')
 170   format(16x,'theta out',
 !  ,6x,'omegax',6x,'omegaz',6x,'rat',6x,'fnorm')
 175   format(18x,' sec. ',6x,' sec. ',6x,' sec. ')
 174   format(/,10x,6f12.5)
 180   format(/,5x,'initial angular offset',/,10x,2f10.2)
 190   format(/,5x,'wire lengths',/,10x,'r7=',f7.3,3x,
 !  'r8=',f7.3,3x,'r9=',f7.3)
       stop
       end
c
c        Subroutine used to rotate top plate
c
       subroutine rotate(xi,yi,zi,xf,yf,zf,omegax,omegaz)
       dimension xi(3),yi(3),zi(3),xf(3),yt(3),zf(3)
       deg=180./(acos(-1.0))
       if((omegax+omegaz).lt.0.00001) then
        do 90 i=1,3
         xf(i)=xi(i)
         yf(i)=yi(i)
         zf(i)=zi(i)
  90    continue
       else
        omegx=omegax/deg
        omegz=omegaz/deg
        omega=sqrt(omegx**2.+omegz**2.)
        ux=omegx/omega
        uz=omegz/omega
        do 10 j=1,3
         xf(j)=xi(j)*((ux**2.)*(1-cos(omega))+cos(omega))
  !     +zi(j)*(ux*uz*(1-cos(omega)))-yi(j)*sin(omega)*uz
        yf(j)=xi(j)*uz*sin(omega)-zi(j)*(ux*sin(omega))
  !     +yi(j)*cos(omega)
        zf(j)=xi(j)*ux*uz*(1-cos(omega))+zi(j)*((uz**2.)
  !      *(1-cos(omega))+cos(omega))+yi(j)*ux*sin(omega)
  10    continue
       endif
       return
       end
c
c        Subroutine used by zscnt
c
       subroutine fcn (x,f,n,par)
       dimension x(n),f(n),par(1)
  !   ,xt(3),yt(3),zt(3)
       common/data/r1,r2,r3,r4,r5,r6,r7,r8,r9,r10,r11,r12
  !   ,xt,yt,zt
```

```
c
      f(1)=((xt(1)-x(1))*x(13)/r7)+((xt(2)-x(4))*x(14)/r8)+((xt(3)
     ! -x(7))*x(15)/r9)
      f(2)=((yt(1)-x(2))*x(13)/r7)+((yt(2)-x(5))*x(14)/r8)+((yt(3)
     !  -x(8))*x(15)/r9)-1.0
      f(3)=((zt(1)-x(3))*x(13)/r7)+((zt(2)-x(6))*x(14)/r8)+((zt(3)
     ! -x(9))*x(15)/r9)
c
      f(4)=(((x(2)-x(11))*(zt(1)-x(3))-(x(3)-x(12))*(yt(1)-x(2)))
     ! *x(13)/r7)
     !  +(((x(5)-x(11))*(zt(2)-x(6))-(x(6)-x(12))*(yt(2)-x(5)))
     !   *x(14)/r8)
     !    +(((x(8)-x(11))*(zt(3)-x(9))-(x(9)-x(12))*(yt(3)-x(8)))
     !     *x(15)/r9)
      f(5)=(((x(3)-x(12))*(xt(1)-x(1))-(x(1)-x(10))*(zt(1)-x(3)))
     !    *x(13)/r7)
     !     +(((x(6)-x(12))*(xt(2)-x(4))-(x(4)-x(10))*(zt(2)-x(6)))
     !      *x(14)/r8)
     !       +(((x(9)-x(12))*(xt(3)-x(7))-(x(7)-x(10))*(zt(3)-x(9)))
     !        *x(15)/r9)
      f(6)=(((x(1)-x(10))*(yt(1)-x(2))-(x(2)-x(11))*(xt(1)-x(1)))
     !    *x(13)/r7)
     !     +(((x(4)-x(10))*(yt(2)-x(5))-(x(5)-x(11))*(xt(2)-x(4)))
     !      *x(14)/r8)
     !       +(((x(7)-x(10))*(yt(3)-x(8))-(x(8)-x(11))*(xt(3)-x(7)))
     !        *x(15)/r9)
      f(7)=(x(1)-xt(1))**2.+(x(2)-yt(1))**2.+(x(3)-zt(1))**2.-(r7**2.)
      f(8)=(x(4)-xt(2))**2.+(x(5)-yt(2))**2.+(x(6)-zt(2))**2.-(r8**2.)
      f(9)=(x(7)-xt(3))**2.+(x(8)-yt(3))**2.+(x(9)-zt(3))**2.-(r9**2.)
c
      f(10)=(x(4)-x(1))**2.+(x(5)-x(2))**2.+(x(6)-x(3))**2.-(r5**2.)
      f(11)=(x(7)-x(1))**2.+(x(8)-x(2))**2.+(x(9)-x(3))**2.-(r4**2.)
      f(12)=(x(7)-x(4))**2.+(x(8)-x(5))**2.+(x(9)-x(6))**2.-(r6**2.)
c
      f(13)=(x(10)-x(1))**2.+(x(11)-x(2))**2.+(x(12)-x(3))**2.-r10**2.
      f(14)=(x(10)-x(4))**2.+(x(11)-x(5))**2.+(x(12)-x(6))**2.-r11**2.
      f(15)=(x(10)-x(7))**2.+(x(11)-x(8))**2.+(x(12)-x(9))**2.-r12**2.
      return
      end
```

APPENDIX C

Planar Stiffness Program

This program calculates the equilibrium position of a four bar mechanism with flexible members on links 2 & 4 and a mass attached to link 3. The user reads in the values for mg, EI, the lengths of links 1, 2, 3, and 4 (r1, r2, r3, & r4) as well as the input angle (thti deg.) for each input state. As with the earlier programs a subroutine is called to solve the 9 constraint equations for the position solution. The program is written in Fortran F77.

```
c Planar analysis with the wires modeled
c as small deflected beams.  3/16/84
c The boundary conditions are pinned at the
c top and clamped at the bottom.
c
c  x1=tho        x4=va          x7=mb
c  x2=ha         x5=vb          x8=da
c  x3=hb         x6=ma          x9=db
c
  program main(input,output,tape5=input,tape6=output)
  dimension x(9),par(1),wk(1000)
  real li,la,lb,lo,mg
  integer i,j
  common u,d,ei,thi,tha,thb,deg,li,la,lb,lo,mg,j
  external fcn,cosh,sinh
c
  pi=acos(-1.0)
  deg=180./pi
  itmax=125
  n=9
c
  read(5,*) mg,ei,d,u
```

```
      ei=4.94e-4
c           Initial estimate for equation solver
      x(1)=0.0
      x(2)=-0.0847
      x(3)=0.0847
      x(4)=mg/2.
      x(5)=mg/2.
      x(6)=0.0
      x(7)=0.0
      x(8)=0.0
      x(9)=0.0
c           User inputs, do (1) times
       read(5,2) 1
2        format(i2)
      do 40 i=1,1
       read(5,*) li,la,lb,lo,thti
       thi=thti/deg
c           Calculate initial angles
       if(i.ne.1) goto 5
        xa=(lo-li)/2.
        tha=asin(xa/la)
        thb=asin(xa/lb)
       5   continue
c           Call equation solver
       call zscnt(fcn,13,n,itmax,par,x,fnorm,wk,ier)
c           Calculate output
       da=x(8)
       db=x(9)
       pha=tha-thi
       phb=thb+thi
       tot=x(1)*deg
c           Calculate input output ratio
       rat=0.0
       if (thti.le.0.0) goto 11
       rat=tot/thti
      11   continue
       xb=li*cos(thi)+lb*sin(phb)-db*cos(phb)
       yb=li*sin(thi)-lb*cos(phb)-db*sin(phb)
       xa=-la*sin(pha)-da*cos(pha)
       ya=-la*cos(pha)+da*sin(pha)
c           Output critical variables
       write(6,20) thti,tot*3600.,rat
       write(6,20) li,lo,la,lb,ei
c 10    format(10x,4e15.4)
       write(6,30) (x(j),j=1,7)
       write(6,30) (x(j),j=8,9)
       write(6,30) xa,ya,xb,yb,pha*deg,phb*deg
      30    format(5x,7f12.5)
      20    format(8x,7f10.4)
       j=0
      40   continue
      stop
      end
```

```
c
c       Subroutine used by zscnt
c
      subroutine fcn (x,f,n,par)
      dimension x(n),f(n),par(1)
      common u,d,ei,thi,tha,thb,deg,li,la,lb,lo,mg,j
      real li,la,lb,lo,ma,mb,mg,ha,hb
      external cosh,sinh
      integer i,j
c
      tho=x(1)
      ha=x(2)
      hb=x(3)
      va=x(4)
      vb=x(5)
      ma=x(6)
      mb=x(7)
      da=x(8)
      db=x(9)
c
      pha=tha-thi
      phb=thb+thi
      b1=sqrt(va/ei)
      b2=sqrt(vb/ei)
      cb1la=cosh(b1*la)
      sb1la=sinh(b1*la)
      cb2lb=cosh(b2*lb)
      sb2lb=sinh(b2*lb)
c
      f(1)=ha*cos(pha)+va*sin(pha)+hb*cos(phb)-vb*sin(phb)
      f(2)=va*cos(pha)-ha*sin(pha)+hb*sin(phb)+vb*cos(phb)-mg
      f(3)=-ma-mb+vb*lo*cos(phb-tho)+hb*lo*sin(phb-tho)
     !      -mg*((lo-u)*cos(tho)/2.+d*sin(tho))
c
      f(4)=ha*sb1la/(b1*cb1la)+ma
      f(5)=hb*sb2lb/(b2*cb2lb)+mb
c
      f(6)=-ha*sb1la/(va*b1*cb1la)+(tho+ha/va)*la-da
      f(7)=-hb*sb2lb/(vb*b2*cb2lb)+(tho+hb/vb)*lb-db
c
      xa=-la*sin(pha)-da*cos(pha)
      ya=-la*cos(pha)+da*sin(pha)
      xb=li*cos(thi)+lb*sin(phb)-db*cos(phb)
      yb=li*sin(thi)-lb*cos(phb)-db*sin(phb)
c
      f(8)=(xb-xa)**2.+(yb-ya)**2.-lo**2.
      f(9)=(yb-ya)/(xb-xa)-tan(tho)
      return
      end
c
c          Evaluate the sinh and cosh in functions
c
      function cosh(a)
```

```
      real a
      cosh=(exp(a)+exp(-a))/2.
      return
      end
c
c
      function sinh(a)
      real a
      sinh=(exp(a)-exp(-a))/2.
      return
      end
```

APPENDIX D
Project Staff in 1983–1984

APPENDIX D

Project Staff in 1983–1984

Faculty

M. M. Barash, Ransburg Professor of Manufacturing and Professor of Industrial Engineering.....	Principal Investigator & Project Director
C. R. Liu, Professor of Industrial Engineering.....	Principal Investigator
K. S. Fu, Goss Distinguished Professor of Engineering (Elec.Eng.).....	Faculty Associate
J. Modrey, Professor of Mechanical Engineering.....	Co–Principal Investigator
A. L. Sweet, Professor of Industrial Engineering.....	Co–Principal Investigator
W. Stevenson, Professor of Mechanical Engineering.....	Faculty Associate
J. J. Talavage, Professor of Industrial Engineering.....	Faculty Associate
R. Hannam*, Visiting Associate Professor of Industrial Engineering.....	Faculty Associate
W. Johnson**, Visiting Professor of Industrial Engineering.....	Faculty Associate
A. Shumsherrudint, Visiting Associate Professor of Industrial Engineering.....	Faculty Associate

(*University of Manchester Institute of Science and Technology, England
**University of Cambridge, England
†Cranfield Institute of Technology, England)

Graduate Research Assistants

P. Chen
Y.C. Chou
P. Ferreira
R. Khanna
S.K. Lee
G.R. Liang
Y.T. Lin
J. Lopez
D. Noller
Y.S. Ouyang
U. Roy
S. Shodhan
R. Srinivasan
S. Venkatramen
R. Venugopal
M.C. Wu
J. York

END

FILMED

11-85

DTIC